Lifetime Measurements for Heavy-Ion-Induced Fission by the Crystal-Blocking Technique

By J. U. ANDERSEN, A. S. JENSEN, K. JØRGENSEN,
E. LÆGSGAARD, K. O. NIELSEN,
J. S. FORSTER, I. V. MITCHELL, D. WARD,
W. M. GIBSON, *and* J. J. CUOMO

Det Kongelige Danske Videnskabernes Selskab
Matematisk-fysiske Meddelelser **40**:7

Kommissionær: Munksgaard
København 1980

Synopsis:

The crystal-blocking technique has been applied to study the time development of fission induced by heavy-ion (^{12}C, ^{16}O, ^{19}F) bombardment of tungsten (and gold). Thin single crystals have been used as targets and the blocking patterns have been recorded with 2-dimensional position-sensitive detectors, which are thin enough ($\sim 20\mu$m) to separate fission fragments from scattered projectiles with the same energy. The blocking dips are analyzed as superpositions of two components, corresponding to short and long lifetimes, and the information extracted is the relative amount of fission with lifetimes $\tau \gtrsim 10^{-16}$ sec. In this analysis, the short-lifetime component is represented by a blocking dip for elastic scattering at lower bombarding energy, which is scaled to the average energy and nuclear charge of fission fragments. The long-lifetime component is represented by a calculated dip. The dependence on bombarding energy of the fraction of fission with long-lifetime has been studied systematically for ^{12}C and ^{16}O bombardment of tungsten in the energy range 80 MeV to 115 MeV. In agreement with expectations based on qualitative considerations, the long-lifetime component initially increases with energy, reaching a maximum of $\sim 20\%$, and then decreases to $\sim 5\%$ at the highest energy. For ^{16}O on W supplementary measurements have been made of the fission cross section for the different W isotopes and of the angular distribution of fission fragments. The results are used together with the lifetime data to determine parameters in a statistical-model calculation of the fission process, which follows the distribution in spin and energy of the fissioning nuclei through the neutron-evaporation cascade. All the experimental results are reproduced with a consistent set of parameter values, and the combination of experimental data turns out to be very effective in constraining the variation of these parameters. In particular, the information obtained from the lifetime measurements on the distribution of fission over stages in the neutron evaporation cascade is important for the interpretation of the measurement of fission-fragment anisotropy, which depends sensitively on the temperature of the fissioning nucleus.

J. U. Andersen, A. S. Jensen, K. Jørgensen, E. Lægsgaard, and *K. O. Nielsen*
Institute of Physics, University of Aarhus, DK-8000 Aarhus C, Denmark.

J. S. Forster, I. V. Mitchell, and *D. Ward*
AECL, Chalk River Nuclear Laboratories, Chalk River, Ontario, Canada.

W. M. Gibson
Department of Physics, State University of New York at Albany, Albany, N.Y. 12222, U.S.A.

J. J. Cuomo
Watson IBM Research Laboratory, Yorktown Heights, NY. 10568, U.S.A.

Printed in Denmark by Bianco Lunos Bogtrykkeri A/S. ISSN 0023-3323. ISBN 87-7304-107-6.

Contents

1. Introduction

The blocking lifetime technique for measurement of nuclear lifetimes in the range ($< 10^{-15}$ s), where nucleon emission dominates the decay of excited nuclei, has been applied to study a variety of processes [1,2]. It is basically a time-of-flight technique which utilizes the fact that displacements of target atoms from lattice sites by more than ~ 0.1 Å can be distinguished by a filling-in of the blocking dip in yield of emitted, charged particles. The method was first established about ten years ago, and from the beginning, investigations of nuclear fission played an important role [3-5]. Systematic studies of neutron-induced fission of uranium isotopes [6-9] have shown that for low excitation energies E*, the lifetime decreases with excitation energy to $\tau \sim 10^{-16}$ s for E* ~ 10 MeV. For higher energies, the lifetime becomes too short to be measured with the technique, and only an upper limit can be established (e.g., $\tau < 10^{-17}$ s for helium-induced fission of ^{238}U at E* = 20 MeV[5]).

An important exception to this behaviour occurs at projectile energies close to threshold for higher-chance fission. It has been observed for both proton bombardment[4] and neutron bombardment[9] of ^{238}U that just above threshold for fission after emission of one neutron (second-chance fission), the blocking dips for fission fragments are filled-in by a slow fission component. Similarly, at higher energies, the fission lifetime would be expected to depend strongly on the average number of neutrons evaporated prior to fission. In fact, only if this number is small ($\lesssim 1$) can the process be usefully characterized by a single lifetime. This problem is crucial for the interpretation of blocking measurements of fission induced by heavy-ion bombardement. Since the heavy ion must have sufficient energy to overcome the Coulomb barrier, the excitation energy will always be high enough to allow evaporation of several neutrons from the compound nucleus.

The pioneering measurements of lifetimes for heavy-ion induced fission were made by Karamyan and co-workers [10,11]. They measured blocking patterns for fission induced by bombardment of tantalum and tungsten crystals with heavy ions (boron, carbon, oxygen, neon, and phosphorus) and identified significant lifetime effects for excitation energies as high as 120 MeV. By assuming that the number of neutrons emitted prior to fission was small, they interpreted these

effects as evidence for a surprisingly long lifetime, $10^{-17} - 10^{-18}$ s, of the initially formed nucleus as compared to expected lifetimes of $10^{-19} - 10^{-20}$ sec. This implies that the nuclear temperature is much lower at high excitation energy than that calculated from a Fermi-gas model with the usual parameter values and, correspondingly, that the level density is much higher than that estimated from such a calculation (see, for example, the discussion by Karamyan et al.[2]).

The present study was stimulated by and is an extension of the work of Karamyan and co-workers. By the use of thin crystal targets, improved angular resolution and statistics, and two-dimensional, position-sensitive semiconductor systems which allow detection of both fission fragments and elastically scattered projectiles, it was felt that additional information on the time evolution of the decay could be obtained. In a preliminary report[12], it was shown that the new results were inconsistent with an interpretation involving delayed decay of the initial compound nucleus. A comparison of blocking dips for fission fragments with blocking dips for elastically scattered ions revealed large effects of compound-nucleus recoil, but a detailed analysis of the shape of these dips showed that the filling-in must be due to a fission component with very long lifetime, $\tau \gtrsim 10^{-16}$ s (with most of the fission occurring within a time too short to be measured, $\tau < 10^{-17}$ s). The long lifetime was interpreted as fission after evaporation of several neutrons, and this interpretation was substantiated by the calculations of Hagelund and Jensen[13], which were prompted by these measurements. Since then, the calculations have been improved[14] mainly by a modification of the analytical level-density expression[15]. We shall present some of the new results and compare them with our data.

The importance of higher-chance fission is also indicated by other types of measurements, e.g., of the angular distribution of fission fragments[16]. It is a simple consequence of the fact that for the systems studied, the neutron-binding energy B_n and the fission barrier B_f are comparable in magnitude. In fig. 1, taken from Huizenga and Vandenbosch[17], the ratio Γ_n/Γ_f, calculated from a Fermi-gas model, is shown as a function of excitation energy for different relative magnitudes of B_n and B_f. The energy dependence is governed mainly by the ratio of Boltzmann factors, $\exp((B_f - B_n)/T)$, where T is the nuclear temperature ($T \propto E^{1/2}$). For $B_n \simeq B_f$, this ratio is almost constant, and fission after evaporation of one or more neutrons will then be as important as first-chance fission.

On the other hand, the fission yield is dominated by first-chance fission in both the limits $B_f \gg B_n$ and $B_f \ll B_n$; in the former limit, the fission probability decreases rapidly with decreasing excitation energy, and in the latter limit, very few compound nuclei survive first-chance fission. Since the fission barrier depends strongly on the fissionability parameter Z^2/A, the variation between these limits can be investigated by a variation of the target-projectile combination.

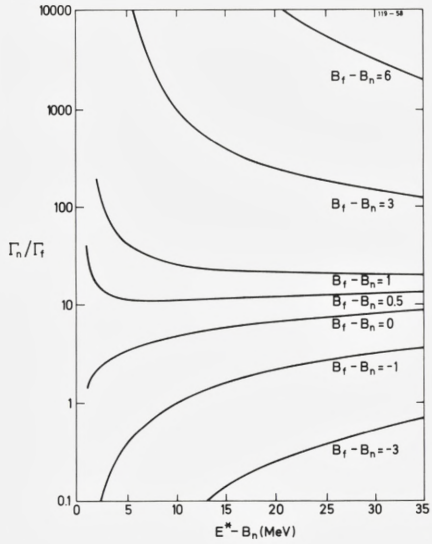

Fig. 1: The dependence of Γ_n/Γ_f on excitation energy for different values of $(B_f - B_n)$. Level-density parameters a_f and a_n were assumed equal to 25 MeV^{-1} and B_n equal to 6 MeV. The figure is taken from ref. 17, with a small correction of notation $(E_f \rightarrow B_f)$.

For a fixed value of Z^2/A, the effective fission barrier may be varied by changing the bombarding energy and thereby the average angular momentum of the compound nuclei. For the very large values of angular momentum attained in heavy-ion reactions, the rotational energy of the compound nucleus may be comparable to the fission barrier. At the saddle point for fission, the moment of inertia is increased by the deformation, and the fission barrier is effectively reduced by the corresponding change in rotational energy, $B_f^{eff} = B_f - \Delta E_{rot}$. The different curves in fig. 1 may therefore also represent different values of angular momentum.

If $B_f > B_n$ for $I = 0$, we may then expect the following variation with bombarding energy: Close to the fission threshold, the yield is dominated by first-chance fission. At somewhat higher energies, the effective fission barrier B_f^{eff}, corresponding to a larger average angular momentum, is reduced to $B_f^{eff} \simeq B_n$ and the contribution from late-stage fission is large. For even higher bombarding energies, $B_f^{eff} < B_n$, and the fission yield is again dominated by the contribution from the first stages of the evaporation chain.

This picture is, of course, greatly simplified. The change in Γ_n/Γ_f with neutron evaporation is not caused by the decrease in temperature alone; other effects such as changes in shell corrections and in the neutron binding energy are also important, but they do not change the qualitative conclusion concerning the energy dependence of the contribution from late-stage fission.

In the present report, we give a detailed account of the experimental investigation. Both from a technical and analytical point of view, it represents a new

development of the crystal-blocking technique. The interpretation of the results in terms of a multi-component time distribution has been established by a large number of measurements with different target thickness, target temperature, crystal orientation, and varying projectile energy. The variation of the magnitude of the long-lifetime component with projectile energy has been measured for oxygen on tungsten in the energy range from 90 to 115 MeV and for carbon on tungsten from 80 to 87 MeV. The results are in qualitative agreement with the simple predictions discussed above.

Detailed numerical calculations of the type introduced by Hagelund and Jensen[13] have been performed. In order to determine some of the parameters in the calculations, we have made systematic measurements of fission cross sections and also of the angular distribution of fission fragments for all four tungsten isotopes (^{182,183,184,186}W) bombarded by ^{16}O in the energy range 90-108 MeV. The combination of such different types of information is found to reduce considerably the ambiguity in selection of parameters for the calculations; in particular, the calculations illustrate the value of the new type of information obtained from blocking measurements.

2. Experimental Details

2.1 *Equipment*

A plan view of the experimental apparatus is shown in fig. 2. Ion beams from the Chalk River MP tandem accelerator entered the target chamber through collimators to produce a beam spot on the target of $\lesssim 0.5$-mm diameter. For the target-detector distances used ($\gtrsim 105$ mm), this resulted in sufficient spatial resolution in the blocking patterns for all target tilt angles and detector angles.

Single-crystal targets (see sec. 2.2) were mounted in a two-axis goniometer which allowed translation of the target in its own x and y frame while preserving the crystal orientation, beam-spot size, and beam-spot position with respect to the detectors. The target-crystal assembly was surrounded by a metal shroud, which was liquid nitrogen cooled to inhibit contamination of the crystal surface. The crystals could also be cooled by heat transfer through a copper braid attached to the rear of the sample holder.

The target chamber and shroud design allowed the detector assemblies to be located in the horizontal plane at any of four predetermined angular settings, viz. $-100°$, $+130°$, and 160-170° on either side of the beam (see fig. 2). Hence, detector pairs could be set to subtend angles of 70° or 90° at the target when we wished to record, simultaneously, two blocking patterns along axial directions of the same symmetry, viz. $<111>$ or $<100>$.

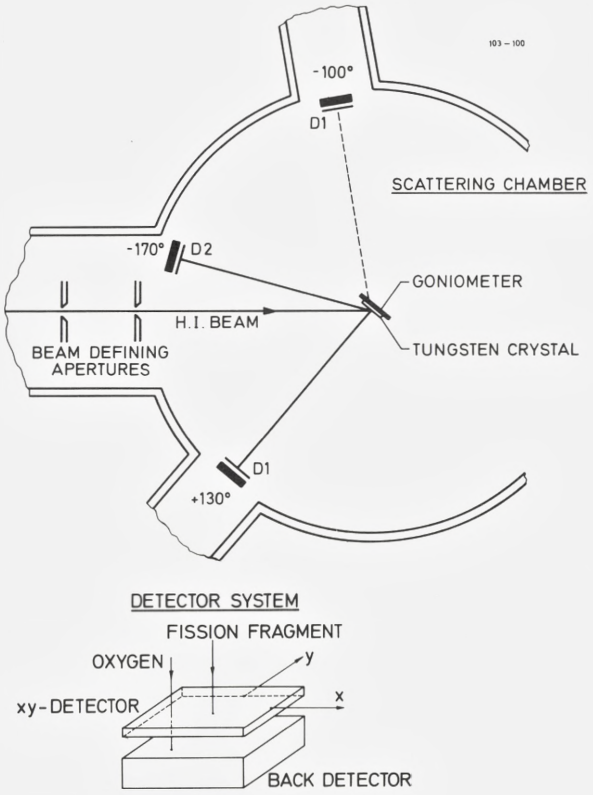

Fig. 2: Plane view of the experimental apparatus. The detectors were placed ~105 mm from the crystal. A detector system, consisting of a position-sensitive front detector and a back detector, is shown separately. The orientation of the crystal corresponds to a blocking angular-distribution measurement around a < 111 > axial direction at 130° to the beam.

2.2 *Crystals*

In contrast to other fission-lifetime measurements based on the blocking technique, thin crystals ($\lesssim 4000$ Å) were used in the present experiments, alleviating uncertainties that arise from depth-dependent cross sections and dechanneling effects. The tungsten crystals were grown epitaxially on Al_2O_3 or MgO, and the gold crystals on NaCl. The use of low-Z-material substrates ensured that there were no troublesome background radiations during heavy-ion bombardment and, consequently, there was no need to remove the crystals from their backings.

Crystal thicknesses were measured by backscattering of 2-MeV He^+ or H^+ beams, and the crystal quality was determined by measuring the minimum yield χ_{min} for 2-MeV He^+ ions incident along a low-index axis. Results for the four tungsten crystals used are shown in table 1. Also shown are the χ_{min} values obtained from 40-MeV ^{16}O-ion blocking dips. The He^+-beam analyses made use of a surface-barrier detector of 15 keV resolution, the χ_{min} values being obtained

Table 1. Properties of the W crystals used in the blocking lifetime measurements. The thickness t, the axis normal to the crystal surface, and the minium yields χ are given. The χ_{He} values were determined as near-surface for channeling of 2.0 MeV ^{4}He particles while the χ_0 values were determined from blocking measurements of 40 MeV elastically scattered ^{16}O ions and are averaged over the crystal thickness.

No.	t[Å]	Axis	χ_{He}	χ_0	Comment
W1	1130	< 110 >	~ 5%	12%	~ 15° off < 110 >
W2	3800	< 111 >	1%	5%	twinned
W3	3350	< 111 >	2%	9%	
W4	570	< 111 >	2%	9%	

from near-surface scattering (see fig. 3). With the oxygen beam, the χ_{min} values were determined from spectra recorded with the modest energy resolution of the detector D1 (see sec. 2.4) and therefore represent averages over the entire crystal thickness. Since depth discrimination was not possible in the fission measurement, these depth-averaged χ_{min} values are the more relevant ones for comparison with blocking of fission fragments.

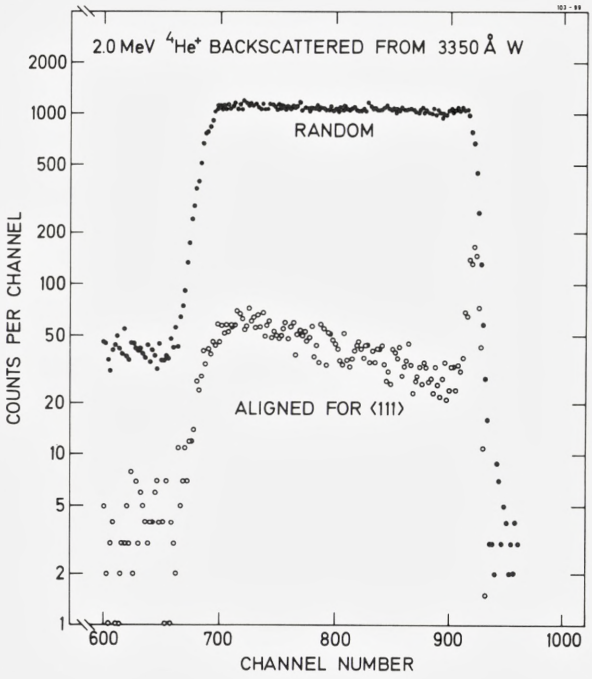

Fig. 3: Spectrum of back-scattered $^4He^+$ ions from the W crystal W3. The closed circles correspond to the case where the beam was incident in a non-channeling direction in the crystal, and the open circles correspond to alignment of a < 111 > axis with the beam direction. The two spectra were recorded for the same number of incident beam particles.

The crystals described in table 1 represent a large variation in thickness, orientation, and quality. The use of such different targets provided an important test of the reproducibility of the observed lifetime effects.

2.3 *Crystal Temperature and Radiation Damage*

At room temperature, the blocking patterns for ^{16}O ions elastically scattered from gold crystals were rather poor, but when the crystals were cooled to ~ 100 K, the elastic blocking patters had much lower minimum yields. Consequently, all fission-fragment blocking measurements with gold were made with the crystals cooled to 100 K. For the tungsten crystals, the χ_{min} values for elastically scattered ^{16}O ions were very good ($\sim$8-10%) at room temperature. Since radiation damage is expected to be worse at lower temperatures, all tungsten measurements except one were made at room temperature.

Radiation-damage effects on the blocking measurement were avoided by translating the crystal at regular intervals. After each 50 μC of accumulated heavy-ion charge, the crystal was translated 0.5 mm, the diameter of the beam as defined by the collimators. This amount of charge was chosen on the basis of measurement with 40-MeV oxygen-ion bombardment, which showed radiation-damage effects in cold gold crystals after 200 μC of accumulated charge. (No distinction is made here between primary radiation damage in the metal film and crystal damage or distortion resulting from radiation damage in the substrate.) For each target position, data accumulation was separated with appropriate markers on the magnetic tape used for data acquisition so that each segment could be evaluated separately for crystal degradation. No evidence of radiation damage was observed.

2.4 *Detectors*

The measurements were made using two specially fabricated silicon-detector systems[18], denoted D1 and D2 in fig. 2. As shown in the lower part of the figure each system consisted of two planar diodes; the front counter had an active area of 14×14 mm^2 and was $\sim 20\mu$m thick. This thickness was sufficient to stop fission fragments but small enough to allow light energetic particles, e.g. elastically scattered ^{16}O, to pass through and be detected in the large-area detector at the back, thus allowing discrimination between fission fragments and the light particles. The front counter was position sensitive in both the x and the y directions[18]. Three signals were obtained from this detector, consisting of the products $E \cdot x$, $E \cdot y$, and $E \cdot (1-x)$. Electronic processing of these three pulses gave signals proportional to energy, x position, and y position. Each signal was encoded by an ADC with

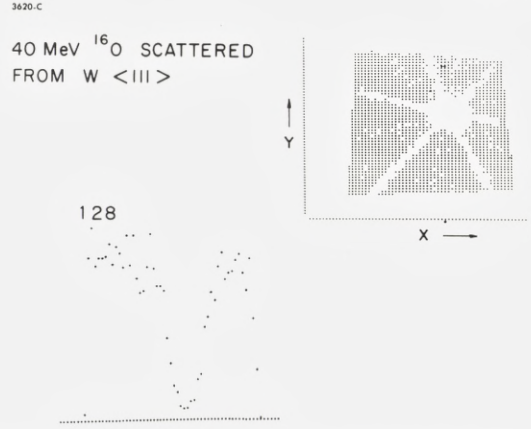

Fig. 4: Photograph of the on-line computer display for 40-MeV ^{16}O bombardment of a W< 111 > crystal. The black dots in the upper right 2-d spectrum correspond to (x, y) channels with a number of counts greater than a preselected minimum value. In the lower left corner, a y scan through the centre of the axial blocking dip is shown; the x value is indicated by a black dot on the x axis.

a conversion range of 256 channels, and the data were written event by event on magnetic tape by the Chalk River PDP-1 computer. A preliminary analysis, in the form of an energy spectrum and a 64 × 64 two-dimensional position spectrum, was made on-line for each detector system. Fig. 4 shows a typical two-dimensional blocking pattern for 40-MeV ^{16}O elastically scattered from a tungsten crystal. The axial and planar minima for this < 111 > direction are clearly visible in the two-dimensional display in the upper right portion of the figure. In the lower left corner is a plot of intensity in the y direction, through the center of the axial dip, for the x position indicated by the dot on the x axis.

The main requirements on the detection system are that it should be able to discriminate fission fragments from all background radiation and to record two-dimensional blocking patterns with high angular resolution. It is possible to satisfy these requirements with the plastic or glass-plate track detectors used in previous blocking-technique measurements of fission lifetimes [10,11], but the experiment control provided by the on-line display and the accessibility of the data for analysis are very important advantages of the present technique.

3. Measurements and Data Reduction

3.1 *Method of Measurement*

Blocking patterns of fission fragments were measured with gold crystals for ^{16}O-ion bombarding energies of 86 and 90 MeV and with tungsten crystals for ^{12}C-ion bombarding energies of 80, 82.5, 85, and 87 MeV, for ^{16}O-ion bombarding energies of 90, 94, 96, 97, 102, 108, and 115 MeV, and for ^{19}F-ion bombarding energies of 95 and 108 MeV. Measurements were also made for elastic scattering of 25-MeV ^{12}C and 25- and 40-MeV ^{16}O-ions.

The tungsten crystal used in the initial measurements (W1) was grown epitaxially with a $< 110 >$ axis nearly perpendicular to its surface. With this axis at 45° to the incident beam, blocking patterns were simultaneously measured for fission-fragment emission along the $< 111 >$ axes at $+170°$ and at $+100°$ to the incident-beam direction. In this geometry, the incident-beam direction, and therefore the compound-nucleus recoil direction, was parallel to a {110} plane. In order to avoid the reduction of yield resulting from channeling of the incident ions, the crystal was tilted slightly (one degree) from the planar direction. Measurements were also made using the same crystal for simultaneous blocking along two $<100>$ axial directions. In this case, one detector was located at $+100°$ and the other at $-170°$ to the incident beam, and the recoil was nearly parallel to a {100} planar direction. As mentioned earlier, the other tungsten crystals used were oriented with a $<111>$ axis normal to the surface. For these crystals, blocking measurements were made sequentially for recoil at 15° and 50° to the $<111>$ axis by orienting the crystal so that the $<111>$ surface normal was directed first at one and then at the other detector, located at the appropriate scattering angles. This method precludes simultaneous measurements of blocking in two directions, but it was found that the results were reproducible. The method has the advantage that while a blocking measurements is being made with one detector, fission fragments striking the other detector emerge from the crystal in a random or non-blocking direction and provide a test of detector response to a uniform exposure. It also allows a free choice of the direction of the recoil relative to the major crystal planes.

3.2 *Data Analysis*

Data analysis was carried out on the Chalk River PDP-10 computer by setting windows on the fission energy spectra and accumulating two-dimensional (64×64) position spectra from the event-mode recorded data. Typical fission energy spectra for 102-MeV ^{16}O and 85-MeV ^{12}C bombardment of tungsten are shown in fig. 5 for detectors located at $-165°$ and $+130°$ to the beam. The energy windows used in the analysis are indicated by horizontal lines with downward pointing arrows at either end. Windows were chosen that were symmetric about the fission peak in the energy spectrum so that a symmetric average over fission-fragment charge and mass, about the mean value, would be taken. This is necessary for comparison of the experimental and calculated blocking patterns since the calculations are made with the average charge and mass for the emitted fragment (see sec. 4). A test of the importance of the spread around the average value was made for the case of 102-MeV ^{16}O bombardment of tungsten, where good statistical accuracy was obtained; analysis of the data with wide and narrow fission

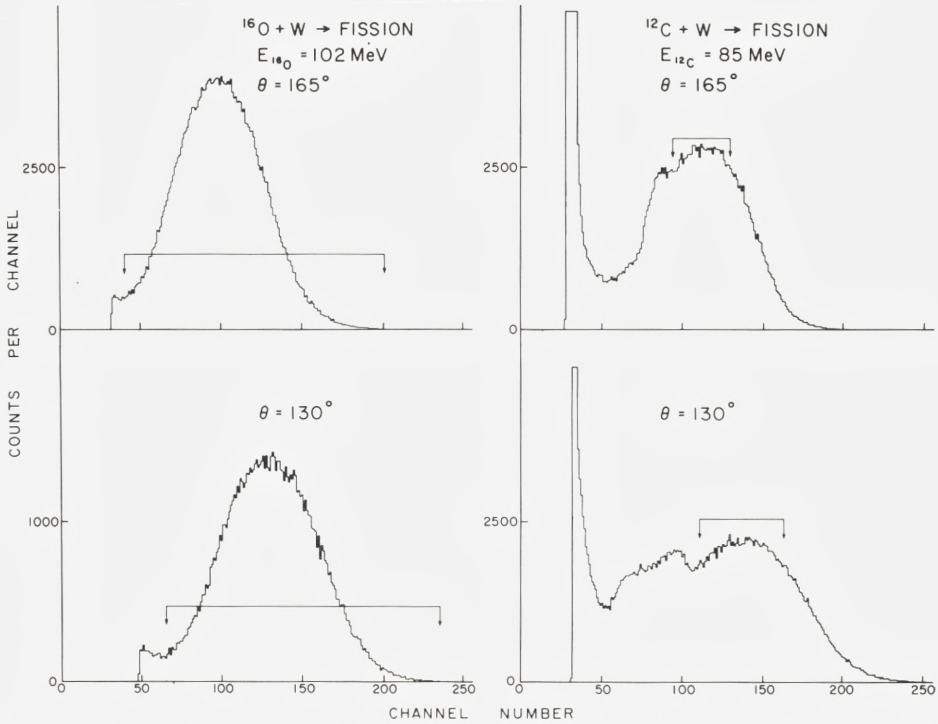

Fig. 5: Fission energy spectra from the position-sensitive front detector for 102-MeV ^{16}O and 85-MeV ^{12}C bombardement of W, for two angles of observation. The horizontal lines with downward pointing arrows indicate the windows used in the analysis to generate the two-dimensional patterns.

energy windows gave blocking patterns which were identical, within statistical errors.

3.3 *Detector Non-Linearities*

With the very thin position-sensitive detectors used in these measurements, there is a problem with non-linearities in the position spectra. These arise from non-uniformities in sheet resistance over the implantation region of the detector and from the compromises required in electronic-shaping time constants[18].

In order to correct the data for non-linearity effects the following correction procedure was applied: Masks, consisting of a thin piece of brass with a square array of holes, 0.5-mm diameter, accurately positioned with 1.5-mm spacing between centres, were placed over each detector. An amorphous tungsten target was bombarded with 40-MeV ^{16}O ions, and two-dimensional position spectra

were recorded for each detector. The centroid, in x and y, for each peak in the two-dimensional spectra corresponding to the holes in the masks was determined by a computer program.

Due to the detector non-linearities, the (x, y) values were not uniformly spaced. The distortion was least-squares fitted by a polynomial which connected the experimental set of (x, y) values with an ideal, uniformly spaced set of (x′, y′) values. The polynomial had the form

$$x = a_0 + a_1 x' + a_2 x'^2 + a_3 y' + a_4 y'^2 + a_5 x' y' + a_6 x' y'^2 + a_7 x'^2 y'$$

and similarly for y with coefficients b_0 to b_7. The number of experimental (x, y) values used in the fitting was usually ~ 80.

The polynomial was used to calculate the position in the distorted spectrum from which to take counts to be put in the corrected two-dimensional spectrum. In general, the position calculated in the distorted spectrum did not have integer (x, y) values, and contributions to the counts transferred to the new spectrum were taken from the four surrounding points with integer coordinate values, weighted according to the distance of the point from the calculated position (x, y). In this way, the integral linearity distortion has been corrected for, and the variation in differential linearity was corrected for separately through multiplication with the local Jacobian of the coordinate transformation.

3.4 *Fission Cross Sections*

In order to aid the interpretation of lifetime distributions, we measured fission cross sections for ^{16}O bombardment of the four tungsten isotopes, $^{182,183,184,186}W$, in a separate experiment. Thin targets ($\sim$100-250 $\mu g/cm^2$) of tungsten oxide, enriched to greater than 98% isotopic purity, on 30-$\mu g/cm^2$ aluminium backings were used. Three thin silicon surface-barrier detectors were placed in a scattering chamber at angles of 100°, 130°, and 170° to the beam direction, and the yield of fission fragments was measured as a function of ^{16}O bombarding energy over the range 90 to 108 MeV. The relative solid angles were determined with a 40-MeV ^{16}O beam using the Rutherford scattering cross section.

The beam current was monitored with a detector at 40°, measuring the elastic-scattering yield. An absolute calibration of the cross sections was obtained by measuring the 40° fission and elastic yield for 97-MeV ^{16}O in one of the fission counters, moved to 40°. The angular distribution of fission fragments was measured in detail for one isotope and one energy (see sec. 3.5) and was assumed to be the same for all energies and isotopes. In fact, the energy dependence of the anisotropy, discussed below, has only a small influence ($< 5\%$) on the evaluation of the total cross sections.

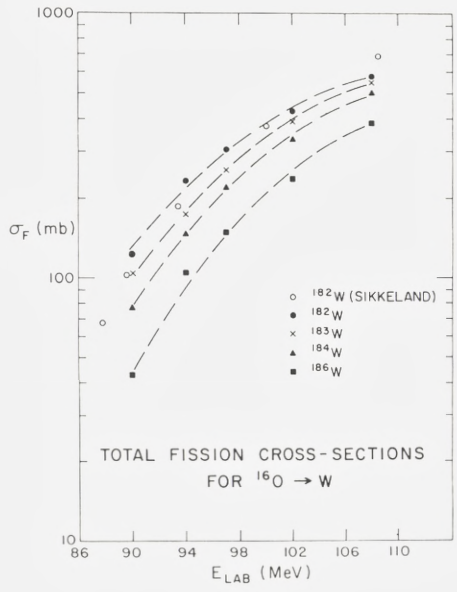

Fig. 6: Measured fission cross sections for ^{16}O-induced fission of the W isotopes, ^{182,3,4,6}W, as functions of ^{16}O bombarding energy. The data of Sikkeland [19] for ^{16}O-induced fission of ^{182}W are also shown.

The measured cross sections are shown in fig. 6 for each isotope as a function of ^{16}O bombarding energy. The results of Sikkeland[19] for ^{182}W, also shown in fig. 6, are consistent with the present data.

3.5 *Fission-Fragment Angular Distributions*

The angular distribution contains important information about the angular momentum and excitation energy of fissioning nuclei, which may be used in the comparison with calculations (see sec. 6). A measurement of the angular distribution of fission fragments, from 40° to 170° in steps of 10°, was made for 97-MeV ^{16}O on ^{183}W, and the results are shown in fig. 7, where angles and solid angles have been converted into the center-of-mass system. As described in the previous section, this measurement allows determination of the total cross section from the yield measured at one angle (if symmetry around 90° is assumed). The limited information for other isotopes and energies obtained in connection with the measurements of cross sections (cf. sec. 3.4) is given in table A4 in the appendix. As a check, a few measurements with a movable counter were made for the isotope ^{182}W. The results are shown in fig. 21 and discussed in sec. 6.4.

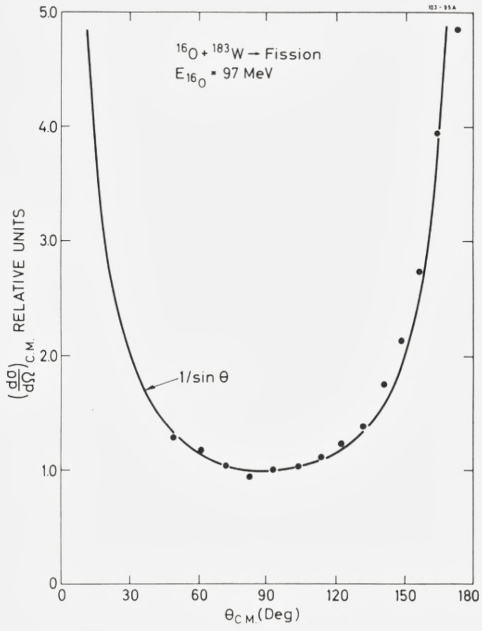

Fig. 7: Fission-fragment angular distribution in the centre-of-mass system for ^{16}O-induced fission of ^{183}W. The experimental angular distribution is compared with a $(\sin \theta)^{-1}$ distribution.

4. Analysis

4.1 *Circular Integration*

As shown in fig. 4, the blocking patterns exhibit strong planar blocking effects in addition to the axial blocking dip. Our analysis is based on the axial dip alone, and in order to eliminate the influence of planar effects, the dip is constructed from circular averages around the minimum. Compared to taking a simple one-dimensional cut through the minimum, this procedure has the advantages of improving statistical accuracy and eliminating planar effects since the planar dips are compensated for by an enhanced yield between planes. On the other hand, by averaging one loses information about asymmetries in the dip associated with lifetime effects.

The first step in the averaging procedure is the determination of the dip centre. We have tried two methods: (i) To search for a minimum number of counts within a small area, and (ii) to determine the centre from the symmetry of the counts at the edges of the dip. The latter procedure is normally more accurate, but it is also more sensitive to detector non-linearities. We have therefore mainly used the first method. A simple measure of the accuracy of the search is the variation of the centre coordinates with the size (radius) of the small area

used in the search. For blocking patterns with reasonable statistics, the accuracy is better than 10% of the half-width at half minimum of the dip. For most purposes, this is sufficient, but if the dip contains structure in the centre (e.g., a flux peak, cf. below), the detailed shape of the circular-averaged dip may depend critically on the centre coordinates. Such structure may be seen more clearly from linear scans through the blocking pattern, as shown in fig. 8.

Normally, the yield as a function of the distance from the centre of the dip is determined from averages over circular rings. For large radii, the rings will intersect the edges of the detector where the yield may be distorted, and these regions are therefore not included in the circular averages. In order to minimize effects of detector non-linearity, the region used for constructing the blocking

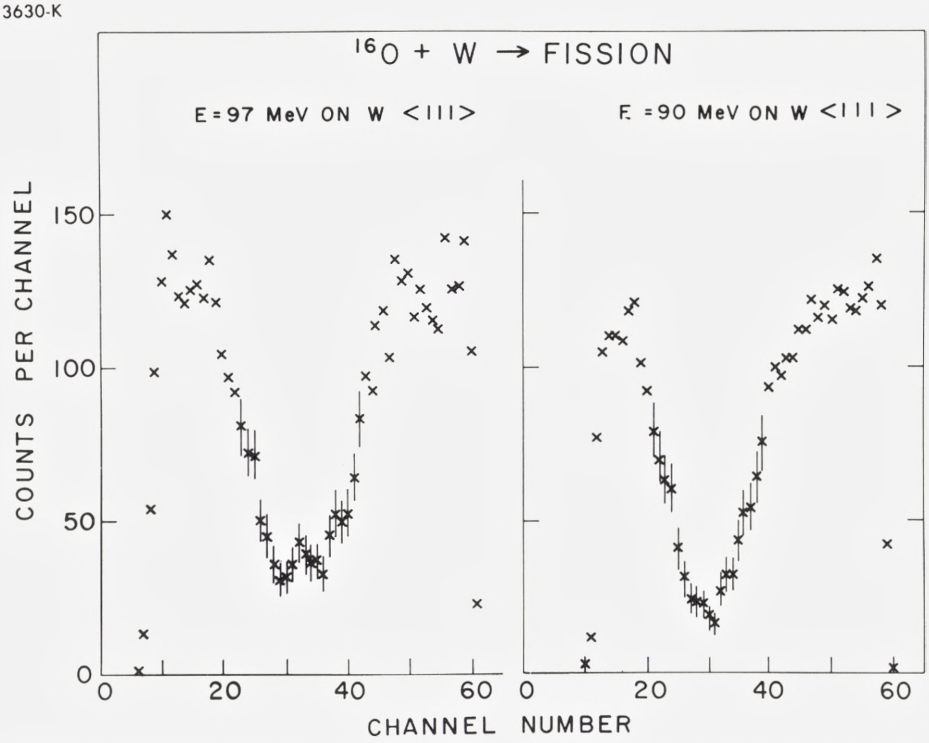

Fig. 8: Linear scans across the 2-d blocking patterns in the < 111 > direction for 90- and 97-MeV ^{16}O-induced fission of W. The 90-MeV data correspond to a recoil direction of the compound nucleus toward the nearest-neighbour < 111 > row of atoms. The 97-MeV data correspond to a recoil directed toward the centre of a < 111 > channel, which results in a "flux peak" in the centre of the blocking dip, as described in the text (cf. figs. 10 and 11).

dip was chosen to be nearly symmetric around the dip centre. A check of distortion due to edge effects or non-linearity is obtained from analysis of 'random' patterns, i.e., two-dimensional spectra containing no strong axial or planar blocking features. In most cases, the circular integration for these spectra gave a yield as a function of distance from the centre coordinates, which was constant within a few percent. In a few cases, we have made a small correction based on the shape of the 'random' spectrum (cf. table 3).

4.2 *Identification of Lifetime Effects*

In order to identify possible effects of a nuclear recoil on the blocking dips, one must compare with a dip obtained in a situation where such effects are known to be absent ('zero-lifetime normalization'). A common method[1] consists of measuring the blocking dips for axes at different angles θ to the incident beam, i.e., to the recoil direction. For small recoil distances, the minimum yield χ of the dip is proportional to the mean-square displacement $<r^2>$,

$$\chi = CNd\pi < r^2 > , \tag{1}$$

where N is the atomic density, d is the spacing of atoms along the axis in question, and C is a constant ($C \simeq 2$-3), which was originally introduced by Barrett[20] to account for deviations from the simple continuum approximation [21] where $C = 1$. For the difference in minimum yield, $\Delta\chi = \chi_1 - \chi_2$, between blocking dips at two different angles θ_1 and θ_2 to the recoil direction, one obtains

$$\Delta\chi = 2CNd\pi v^2\tau^2(\sin^2\theta_1 - \sin^2\theta_2) . \tag{2}$$

Here, v denotes the recoil velocity, τ the lifetime, and we have assumed the decay to be exponential. In this way, the contribution to $<r^2>$ from thermal vibrations is eliminated. Also, other contributions to the minimum yield from, e.g., dechannelling or crystal imperfections, are strongly reduced.

This type of analysis has been applied to the lifetime investigation of heavy-ion-induced fission by the Dubna group[10,11], and substantial lifetime effects have been observed. However, our measurements do not show any significant dependence of the minimum yield on the angle θ between the recoil direction and the axis [12]. This is illustrated by the results for 96-MeV ^{16}O on tungsten shown in the upper part of fig. 9. A substantial influence on the dip of a nuclear recoil is revealed only by a comparison to the blocking dips obtained for elastic scattering of 40-MeV oxygen. In the figure, these dips have been scaled in angle by a factor $(Z_{ff}/Z_O)^{1/2} \cdot (E_O/E_{ff})^{1/2}$, where Z and E denote nuclear charge and energy of fission fragments and of scattered oxygen. The average fission-fragment energy E_{ff} is calculated from published values of the energy release in fission[22].

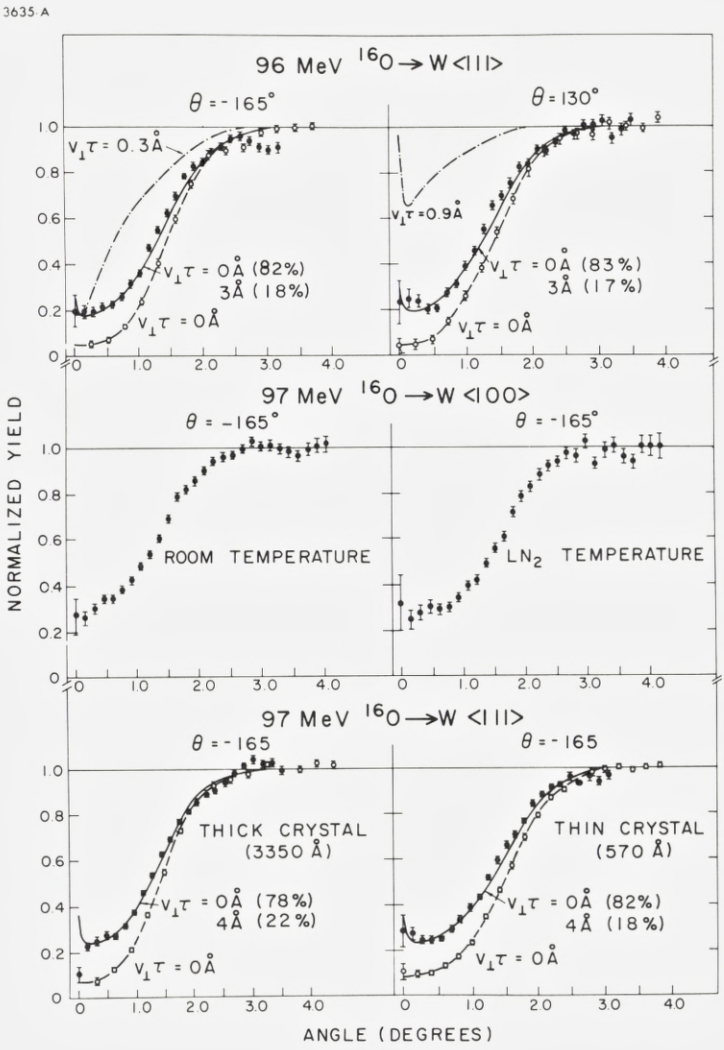

Fig. 9: Fission-fragment blocking dips (closed circles) for 96- and 97-MeV ^{16}O bombardment of W. Results are shown for different angles θ between the incident beam and the axis, different crystal temperatures, and different crystal thicknesses. Also shown, as open circles, are blocking dips for 40-MeV ^{16}O elastic scattering, scaled in angle by $(Z_{ff}/Z_o)^{1/2} \times (E_o/E_{ff})^{1/2}$ (see text). Included in the 96-MeV plots are predicted blocking dips for $v_\perp\tau = 0.3$ Å and 0.9 Å. Solid lines through the data points are fits with the indicated amounts of short- and long-lived fission components.

The elastic minimum yields are seen to be lower by ~ 0.15. The middle and lower pairs of measurements in fig. 9 demonstrate that this difference is not caused by a difference in multiple scattering for fission fragments and oxygen. A decrease in crystal temperature to liquid-nitrogen temperature strongly reduces scattering due to thermal vibrations, and as shown in the middle part of fig. 9, the $<100>$ dip for fission fragments becomes wider, but the minimum yield is nearly unaffected. Neither does the variation of the crystal thickness by a factor of 6 change the difference between minimum yields for fission fragments and elastically scattered oxygen, as shown in the lower pair of blocking dips in fig. 9. We interpret this difference in the minimum yield as being due to a fission component with a lifetime so long that the corresponding average recoil distance perpendicular to the blocking axis is large, even for $\theta = -165°$. It can be seen from fig. 9 that the dips are consistent with this interpretation. The solid line through the data points has been obtained by a superposition of dips corresponding to a short lifetime ($v_\perp \tau = 0$) and a long lifetime ($v_\perp \tau = 2$ or 3 Å). The short-lifetime dip is obtained from elastic scattering of oxygen, scaled as indicated above, and the long-lifetime dip from the calculation described below. This interpretation is consistent with all our data.

4.3 *Calculation of Dips*

The dependence of the blocking dip on the average recoil distance has been calculated in the "statistical-equilibrium multistring" approximation[1]. We shall first describe the model and present some results and then discuss briefly the accuracy and limitations of such a calculation.

The first assumption is that the trajectories of the emitted fission fragments may be described as motion in a transverse potential obtained by averaging the crystal potential along the axial direction. This is normally denoted the continuum approximation [21,23]. With sufficient accuracy, we may represent the potential from a string of atoms by the standard potential of Lindhard[21],

$$U(r) = \frac{Z_1 Z_2 e^2}{d} \log((Ca/r)^2 + 1) . \qquad (3)$$

Here, Z_1 and Z_2 are the nuclear charges of the particle and the crystal atoms, respectively, d is the atomic spacing in the string, r is the perpendicular distance from the string, and a is the Thomas-Fermi screening distance, $a = a_0 0.885 (Z_1^{2/3} + Z_2^{2/3})^{-1/2}$, where a_0 is the Bohr radius. The constant C is a potential parameter, which is normally taken to be $C = \sqrt{3}$. It is convenient to introduce a characteristic angle ψ_1, by

$$\psi_1 = \left(\frac{2Z_1 Z_2 e^2}{Ed}\right)^{1/2}, \tag{4}$$

where E is the particle energy. Combining eqs. (3) and (4) gives

$$U(r) = \tfrac{1}{2} E\psi_1^2 \log\left((Ca/r)^2 + 1\right). \tag{5}$$

The total crystal potential is taken to be the sum of single string potentials. In the following, this sum i denoted by U. Since the potential decreases rapidly at large distances, only a few strings need be included. Fig. 10 shows contour plots of the multistring potential for a < 111 > direction in tungsten.

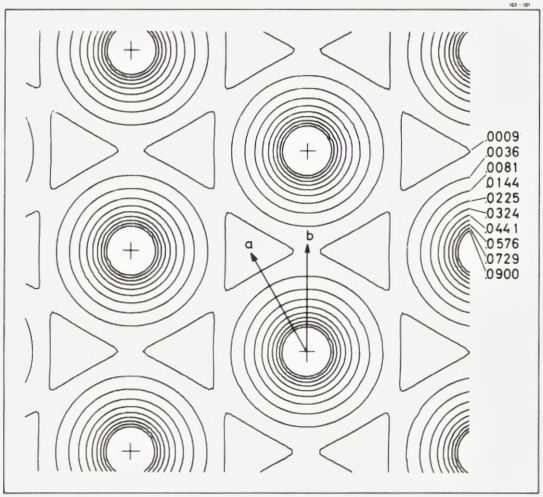

Fig. 10: Continuum potential-energy contours for fission fragments (Z = 41, A = 100) channeled along the < 111 > direction in W. The contours correspond to constant steps in ψ, and the numerical values shown express $E\psi^2$ in units of $E\psi_1^2$ The two recoil directions indicated by arrows a and b correspond to the two linear scans in fig. 8. The centers of atomic strings are marked by crosses. The distance between centers is 2.58 Å.

For a particle moving in this potential, the transverse energy $E_\perp = E\varphi^2 + U(\bar{r})$ will be conserved. Here φ is the instantaneous angle of motion with respect to the string direction and $\bar{r}$ is the position in the transverse plane. The motion of a particle with a given transverse energy $E_\perp$ is restricted to the area in the transverse plane $U(\bar{r}) < E_\perp$, i. e., bounded by the contour corresponding to $U(\bar{r}) = E_\perp$. In statistical equilibrium, the particle is found with equal probability anywhere in this area[21],

$$P(\bar{r}) = \begin{cases} 1/A(E_\perp) & \text{for } U(\bar{r}) < E_\perp \\ 0 & \text{for } U(\bar{r}) > E_\perp \end{cases}, \tag{6}$$

where $A(E_\perp)$ is the allowed area (per unit cell).

Assuming statistical equilibrium, we may write an expression for the probability for particles emitted inside the crystal (isotropically) at position $\bar{r}$ in the transverse plane to emerge from the crystal at an angle ψ to the axis,

$$\Pi(\bar{r},\psi) = \int_{U(\bar{r})}^{\infty} dE_\perp \frac{1}{A(E_\perp)} \int d^2\bar{r}' \delta(E\psi^2 + U(\bar{r}') - E_\perp) . \quad (7)$$

This probability or yield is normalized to unity in the random case, i.e., for $U(\bar{r}) \equiv 0$.

Performing the integration over $E_\perp$, we obtain

$$\Pi(\bar{r},\psi) = \int d^2\bar{r}' \frac{1}{A(E\psi^2 + U(\bar{r}'))} \Big|_{E\psi^2 + U(\bar{r}') > U(\bar{r})} \quad (8)$$

If the emitting nucleus is recoiling, with a transverse direction specified by a unit vector $\bar{e} = (e_x, e_y)$, expression (8) must be averaged over the one-dimensional distribution $f(r)$ of points $\bar{r} = r\bar{e}$, and the total yield at angle ψ becomes

$$P(\psi) = \int_0^{\infty} dr f(r) \Pi(r\bar{e},\psi) . \quad (9)$$

For exponential decay with lifetime τ and recoil velocity $v_\perp$ perpendicular to the axis, we have

$$f(r) = \frac{1}{v_\perp \tau} e^{-r/v_\perp \tau} . \quad (10)$$

We have neglected the thermal vibrations, which is reasonable if $v_\perp \tau \gg u_1$, where u_1 is the one-dimensional RMS vibrational amplitude. For $v_\perp \tau \gtrsim u_1$, a simple correction to eq. (9) consists in replacing $\bar{r} = r(e_x, e_y)$ by $(((re_x)^2 + u_1^2)^{1/2}, ((re_y)^2 + u_1^2)^{1/2})$. This correction has been included in the numerical calculations presented below (fig. 11).

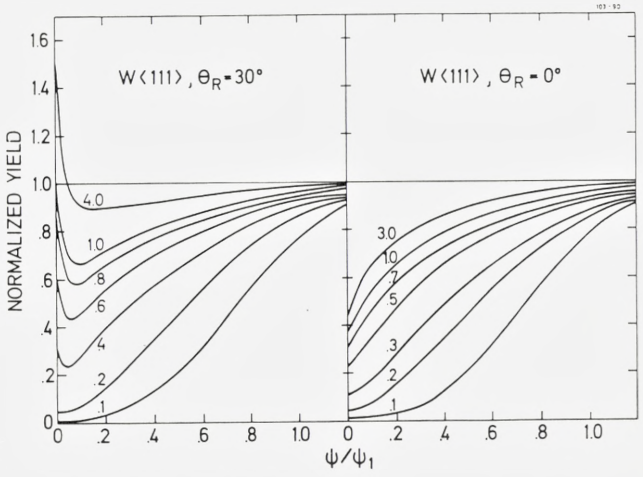

Fig. 11: Calculated blocking dips for fission fragments along a <111> axis in W, using the continuum potentials shown in fig. 10. Blocking dips are shown for recoil angles, θ_R, of 0° and 30° between the transverse component $\bar{v}_\perp$ of the recoil velocity and the direction to the nearest-neighbour string (directions b and a in fig. 10), and the values of $v_\perp \tau$ (in Å) are indicated.

The formulae (8)-(10) lend themselves readily to numerical evaluation. The main job is the construction of tables for the functions U and A. By using symmetry arguments, the evaluation may be restricted to a small fraction of the unit cell. The contour plots of the potentials shown in fig. 10 were calculated by the computer program used to evaluate the blocking dips shown in fig. 11. For comparison, it should be noted that the width of an elastic dip ($v_\perp \tau = 0$) is $(\psi_{1/2}/\psi_1) \sim 1$. For small average displacements, the main effect on the dip is a narrowing, while for larger displacements, the increase in minimum yield is the dominant feature. For $v_\perp \tau \gtrsim 2$ Å, there is virtually no dependence on the magnitude of $v_\perp \tau$.

The recoil directions for the two sets of curves shown in Fig. 11 are specified by the values of θ_R, which is the angle between the projection of the recoil direction on the transverse plane and the direction to the nearest neighbouring string (cf. fig. 10). The values of θ_R have been chosen to correspond to the measurements presented in the following section. For $\theta_R = 30°$, the recoil is towards the centre of the channel where the potential has a minimum. Fission fragments emitted there give rise to a sharp peak at very small angles. This phenomenon was first observed in measurements of the location of interstitial impurities by the channeling technique[24]. It may be noted also that calculations very similar to those presented above have been used to interpret other such measurements[25]. The importance of the recoil direction for nuclear-lifetime measurements was first pointed out by Hashimoto et al.[26].

Finally, a brief comment on the accuracy expected from these calculations. The two basic approximations applied are conservation of transverse energy and statistical equilibrium in the transverse phase space for fixed transverse energy. For thin targets, the first approximation is violated mainly by fluctuations in scattering by a string, due to thermal vibrations of the string atoms. This effect will be strong only for large transverse energies when the particle can penetrate close to the centre of strings, i.e., to distances comparable to the vibrational amplitude[27]. The elastic blocking dip ($v_\perp \tau = 0$) will be very sensitive to this thermal multiple scattering, but for values of $v_\perp \tau$ where the predicted blocking dip is significantly narrower than the elastic one, the sensitivity is much smaller [1,28]. The second approximation of statistical equilibrium is not expected to be strictly fulfilled, and indeed it is a very interesting possibility that one may be able to derive information about the magnitude of the nuclear recoil from asymmetries of the blocking dip. By performing the circular averaging, however, one eliminates such asymmetries and effectively imposes an equilibrium in momentum space. It is expected, therefore, that even for relatively thin crystals, the assumption of statistical equilibrium is a good approximation for calculations of the azimuthally averaged blocking dips.

4.4 *Fitting Procedure*

As illustrated in fig. 9, the measured blocking dips have been fitted by a superposition of two components, a long-lifetime component represented by a calculated curve and a short-lifetime component ($v_\perp \tau = 0$) represented by the scaled blocking dip for elastic scattering. The advantage of using the elastic dip for zero-lifetime normalization is that the influence of crystal imperfections, including thermal vibrations, is taken into account. The question is, however, how accurate the simple scaling is. Consider first the scaling of the halfwidth of the dip. For a perfect crystal without thermal multiple scattering, this scaling should be accurate for high projectile energies. More precisely, the condition[23,29] is that

$$\varrho/(\psi_1 d) > 1\,, \tag{11}$$

where we have used the symbol ϱ for the two-dimensional vibrational amplitude, $\varrho = \sqrt{2}u_1$. This condition is only marginally fulfilled for the fission fragments, but the deviation from scaling should be small[28]. Because of thermal multiple scattering, the width of a blocking dip varies fairly rapidly with crystal thickness for small thicknesses[30]. This effect is not identical for elastic scattering of 40-MeV oxygen and for fission fragments since the characteristic depth z_n for thermal scattering depends[21] on the magnitude of the characteristic scattering angle ψ_1 given by eq. (4), $z_n \propto \psi_1^{-2}$. However, the effect should be small. The halfwidths for the blocking dips for elastically scattered oxygen are all very close to ψ_1 (within $\sim 5\%$), and the halfwidth estimated from the standard potential is, in the absence of multiple scattering[21],

$$\psi_{1/2} = \psi_1 [\tfrac{1}{2} \log ((Ca/\varrho)^2/\log 2 + 1)]^{1/2} = 1.08\psi_1 \tag{12}$$

at room temperature, where $\varrho \sim 0.07$ Å[31]. Thus the reduction caused by thermal scattering is $\lesssim 10\%$. We may also note that the dependence of the half-width, eq. (12), on the screening length a is weak, and therefore the variation of the scaling factor in eq. (12) with Z_1 is very small.

Other factors affecting the accuracy of the scaling are the large energy spread for fission fragments (cf. fig. 5) and the influence of angular resolution, which will depend on the width of the blocking dip. Such effects only become important if a very detailed interpretation of the shape of the blocking dip is attempted. Our analysis is based on simple two-component fits and the accuracy of the scaling of the width of the elastic dip seems sufficient for this purpose. In particular, the lower pair of measurements in fig. 9 shows that the angular scaling is not much affected by multiple-scattering effects.

Scaling of the minimum yield is also supported by the measurements for very different crystal thickness. Multiple-scattering effects are expected to be somewhat stronger for fission fragments than for backscattered 40-MeV oxygen, and

the observation of fission dips with a minimum yield almost identical to that of the corresponding elastic dip (see sec. 5) is therefore another strong indication that the scaling of the minimum yield is reasonably accurate. The magnitude of the minimum yield depends on the quality of the thin single crystals used as targets (cf. table 1), and one of the advantages of using the elastic dips for zero-lifetime determination is that effects due to crystal imperfection are largely cancelled. It is necessary also to correct the calculated dips for these effects, and in the fits we have replaced the calculated yield function Y_c by $Y_c(1-\chi_{el})+\chi_{el}$, where χ_{el} is the measured minimum yield for the elastic blocking dip. This correction becomes important when an intermediate-lifetime component ($0.1\,\text{Å} < v_\perp\tau < 1\,\text{Å}$) is included in the analysis.

Some comments about the selection of parameters for the fits are also in order. First, normalization of the fission dip was treated as an adjustable parameter. In some cases, the random level is not very well established, and the normalization may appear to be wrong (cf. upper left corner in fig. 9). However, at large angles, the circular average includes regions close to the detector edge, and spurious structure due to detector non-linearity may appear. For these cases, we found similar structure in an analysis of the corresponding blocking pattern taken for a random direction, using the same dip centre. Second, the average recoil distance $v_\perp\tau$ for the long-lifetime component was chosen; detailed arguments for the specific choices will be given later. Third, an upper limit on the angular range for fitting was specified. For the simple two-component fits, the first six points in the bottom region of the dip were selected, thus emphasizing agreement in minimum yield. The computer program determined the relative magnitudes of the two components, which gave the lowest value of χ^2 over that angular region. For most cases, the uncertainty in the determination of the magnitude of the long component was ~1-2%. Thus, the two upper dips in fig. 9 correspond to the same magnitude of the long component, and the difference between the long-lifetime components for the two lower dips is barely significant.

5. Data Presentation

5.1 *Data for* $^{16}O \rightarrow Au$

In the first series of measurements, fission induced by oxygen bombardment of gold crystals was investigated. At that time, we were still looking for a dependence of the minimum yield on the angle θ between the recoil direction and the blocking axis (cf. sec. 4.2). The blocking dips for fission fragments were measured along two <110> directions at approximately $+170°$ and $-100°$ to the beam direction, respectively. Results for four different runs are shown in table 2. For each dip,

Table 2. Minimum yields of fission-fragment blocking dips for ^{16}O induced fission of ^{197}Au at observation angles of $-100°$ and $170°$ to the beam. The minimum yields χ are determined by the counts contained within the circle with the specified radius, normalized to the random level of the blocking dip. The radius and the half angle $\psi_{1/2}$ of the blocking dips are given in units of channels in the 2-d spectrum. $\Delta\chi$ is the difference in minimum yield between the forward and backward counters.

Energy (MeV)	Angle (deg)	Radius	χ(%)	$\psi_{1/2}$	Angle (deg)	Radius	χ(%)	$\psi_{1/2}$	$\Delta\chi$(%)
90	170	2.5	14.0 ± 2.2	9.0	-100	2.0	13.5 ± 3.0	7.3	-0.5 ± 3.5
		5.0	20.0 ± 1.3			4.0	19.5 ± 2.0		-0.5 ± 2.4
90	170	2.5	17.5 ± 1.4	9.7	-100	2.0	18.3 ± 2.0	7.3	0.8 ± 1.8
		5.0	22.5 ± 0.8			4.0	23.0 ± 1.1		0.3 ± 1.4
86	170	2.5	13.4 ± 1.9	9.0	-100	2.0	16.7 ± 3.1	7.5	3.3 ± 3.6
		5.0	16.9 ± 1.0			4.0	20.6 ± 1.5		3.7 ± 1.8
86	170	2.5	14.7 ± 2.3	9.5	-100	2.0	14.2 ± 3.1	7.9	-0.7 ± 3.9
		5.0	19.8 ± 1.3			4.0	19.3 ± 1.7		-0.5 ± 2.2

two values of the minimum yield χ are given. They have been obtained by averaging the counts in the centre of the dip within a circle with a diameter equal to 25% and 50% of the full width at half maximum of the dip. The uncertainties are based on counting statistics only. For both bombarding energies, the difference $\Delta\chi$ is zero within an error of two percent.

Unfortunately, we did not at that time use a zero-lifetime calibration based on elastic scattering of oxygen, but from a comparison with the minimum yield for backscattering of 2-MeV helium ($\chi \simeq 7\%$ averaged over the crystal thickness), we may conclude that a possible long-lifetime component must contribute less than 10% to the fission yield. A difference between the shapes of the blocking dips for the two bombarding energies does suggest the presence of a long-lifetime component, at least for E = 90 MeV.

5.2 *Data for* $^{16}O \rightarrow W$

The experiments with tungsten targets have all been analyzed as discussed in secs. 3 and 4, and the results are given in table 3. The quality of the two-component fits may be judged from figs. 12 and 13, which show results from two different runs with different target crystals. The data in fig. 12 were obtained with the two $<111>$ axes in the directions of the two detectors simultaneously, while the blocking dips shown in fig. 13 were obtained separately for different crystal tilts.

In most cases, the two components chosen for the fit correspond to very short and very long recoils. Only for E = 90 MeV does the dip at $\theta = -165°$ indicate the presence of a significant component with an intermediate lifetime. The three

3635 C

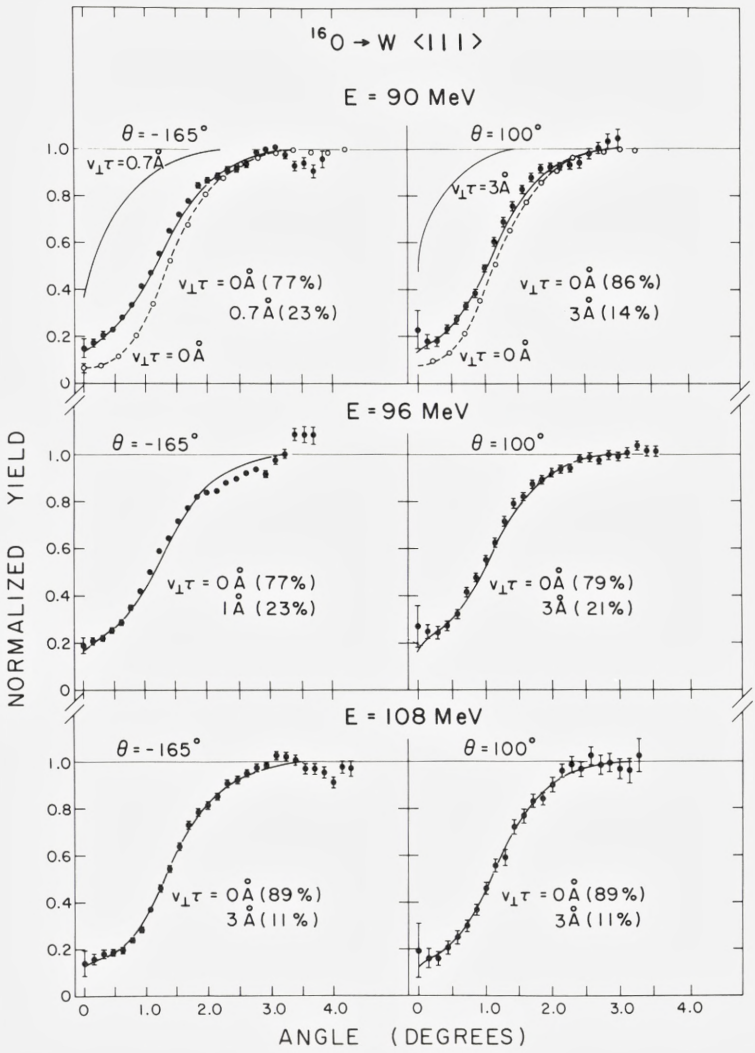

Fig. 12: Fission-fragment blocking dips (closed circles) for 90-, 96-, and 108-MeV ^{16}O bombardment of W. The recoil angle is $\theta_R = 0°$ (direction b in fig. 10). The solid curves are fits by a superposition of two components with different average recoil distances $v_\perp\tau$ (see text). For 90-MeV are shown the blocking dips for 40-MeV ^{16}O elastic scattering (open circles) scaled in angle and the calculated dips for a long average recoil (upper solid curve), which represent the two components in the fit.

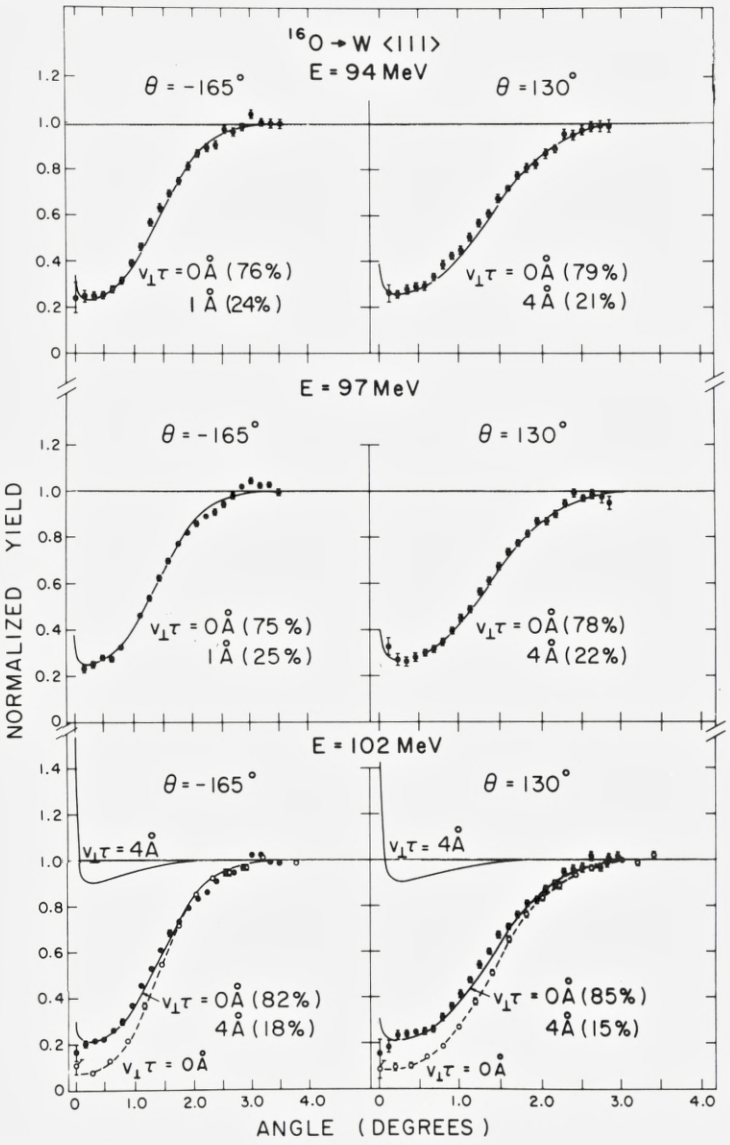

Fig. 13: Fission-fragment blocking dips for 94-, 97-, and 102-MeV bombardment of W for $\theta_R = 30°$ (direction a in fig. 10). The solid lines through the data are two-component fits, and the two components are shown for 102 MeV (cf. caption to fig. 12).

Energy (MeV)	Crystal	Det. Angles	$v_\perp\tau$(Å)	Amount χ_L(%)
90	W1	−165	0.7	20.6 ± 1.4
			0.5	23.5 ± 1.7
90	W1	−165	0.7	22.9 ± 0.5
			0.5	26.0 ± 0.7
		−100	2.0	14.9 ± 1.2
			3.0	15.0 ± 1.2
94	W3	−165	1.0	23.5 ± 0.6*
			4.0	20.3 ± 0.6*
		130	4.0	21.4 ± 0.9
96	W1	−165	1.0	25.8 ± 1.0
			3.0	23.2 ± 0.8
		−100	3.0	17.0 ± 3.1
96	W1	−165	1.0	23.1 ± 0.2
		−100	3.0	22.3 ± 1.4
96	W1	−165	1.0	19.7 ± 1.2
		−100	3.0	22.1 ± 4.6
96	W2	−165	1.0	21.5 ± 0.8
			3.0	18.4 ± 0.8
		130	3.0	16.8 ± 1.0
97	W3	−165	1.0	24.4 ± 0.4*
			4.0	21.5 ± 0.3*
		130	4.0	21.9 ± 0.8
97	W3	−168	1.0	23.3 ± 0.9
			4.0	19.8 ± 0.6
		160	1.0	21.3 ± 0.9
			4.0	18.2 ± 0.7
97	W4	−165	2.0	18.3 ± 0.5
			4.0	17.4 ± 0.5
102	W3	−165	4.0	17.9 ± 0.2*
		130	4.0	15.4 ± 0.6
108	W1	−165	3.0	10.9 ± 0.6
		−100	3.0	10.9 ± 2.4
108	W3	−165	4.0	13.7 ± 1.2
		130	4.0	10.7 ± 0.6
115	W3	−165	4.0	5.8 ± 0.5
		130	4.0	4.1 ± 1.8

Table 3. Results of two-component fits to W(^{16}O, f) data. The beam energy and crystal identification are given in the first two columns (cf. table 1 for characterization of crystals), and in the third column

the angle of the detector to the beam direction is specified. The blocking dips are fitted with a superposition of two components, one with a short lifetime, $v_\perp\tau = 0$, and one with the average perpendicular recoil distance given in the fourth column. The magnitude of this long-lifetime component χ_L is given in the last column, with an error corresponding to an increase of unity in χ^2 for the fit. For some cases, two equally good fits are given. Note that different choices of $v_\perp\tau \gtrsim 2$ Å are equivalent, i.e., a blocking dip corresponding to very long lifetimes may be represented by any value $v_\perp\tau \gtrsim 2$ Å. For the cases marked with an asterisk, the magnitude of χ_L obtained from the fit was increased by 2% as a correction for nonlinearity. Also the corresponding numbers in figs. 9 and 13 have been corrected.

measurements at 90 MeV are all fitted well with a long component with recoil $v_\perp\tau = 0.7$ Å for the backward detector (table 3, one result given in ref. 12). The corresponding recoil for the forward counter is larger by a factor of ~ 4, i.e., close to 3 Å.

For the intermediate energies, 94-97 MeV, a recoil of $v\tau \simeq 4$ Å, corresponding to $v_\perp\tau \simeq 1$ Å for the backward detector, has been chosen for the fits shown in the figures. The arguments for this choice are not very strong, and the dips can be fitted equally well with $v_\perp\tau = 4$ Å for the backward counter. As seen in the table, this changes the magnitude of the long component by $\sim 2\%$. The choice of the value of $v\tau \sim 4$ Å is based on analysis of fine structure in the dips, which for these energies shows evidence of asymmetries correlated with the recoil direction.

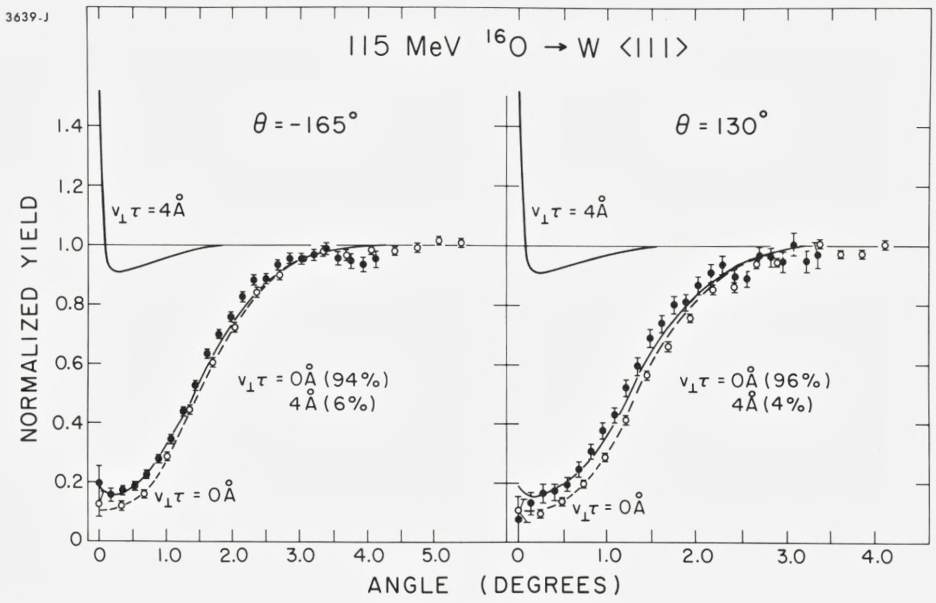

Fig. 14: Fission-fragment blocking dips for 115-MeV ^{16}O bombardment of W for $\theta_R = 30°$. Also shown are the short- and long-recoil dips used in the fit.

From table 3 it can be seen that the magnitude of the long component varies systematically with energy, and different measurements at the same energy are reasonably consistent. The errors given in the table are based on the χ^2 analysis and do not include uncertainties associated with the determination of a random level (normalization) or of the elastic dip. At the high bombarding energies, the magnitude of the long component approaches zero. The results and analysis of the measurements at 115 MeV are shown in fig. 14. The fact that the fission dips for some cases are close to the scaled elastic dip is a crucial check of the method of analysis, as discussed in sec. 4.4.

5.3 *Dependence on Recoil Direction*

The measurements shown in figs. 12 and 13 correspond to two different recoil directions. As discussed in sec. 4.3, the central structure of the blocking dips will, for long recoil distances, depend on whether the recoil is directed towards the centre of the channel (fig. 13) or is parallel to the side of the channel (fig. 12), and the calculated dips for these two situations are shown in fig. 11. The data in the two figures are not in all cases consistent with the predicted structure. This may at least partly be due to the difficulty of locating the centre of the dip. A change in centre coordinates by one channel, which is about the uncertainty of the determination, may in some cases lead to a significant change in the central structure of the circular averaged dip. A better check of the predicted dependence on recoil direction is obtained from linear scans through the dip centre. Such scans, corresponding to the two different recoil directions, are shown in fig. 8. The peak due to flux peaking in the centre of the scan for 97 MeV is clearly indicated, while for the 90-MeV scan, there is a narrow dip in the centre. For the measurements shown in fig. 12, the recoil is parallel to a side of the channel, but the data do not confirm the predicted narrow dip at the centre for the forward counter ($\theta = 100°$). A possible explanation for this discrepancy may be that the recoil direction for compound nuclei fissioning after evaporation of several neutrons is affected by the neutron emission, and the angular distribution will have a width of a few degrees. This may influence the central structure if the recoil is very long. It is then important also to consider whether the recoiling atoms may be deflected by neighbouring atoms, but this appears not to be the case for the geometry of the present measurements.

5.4 *Data for* $^{12}C \rightarrow W$ *and* $^{19}F \rightarrow W$

The measurements presented in table 3 demonstrate the disappearance of the long-lifetime component at high bombarding energies, as predicted from the

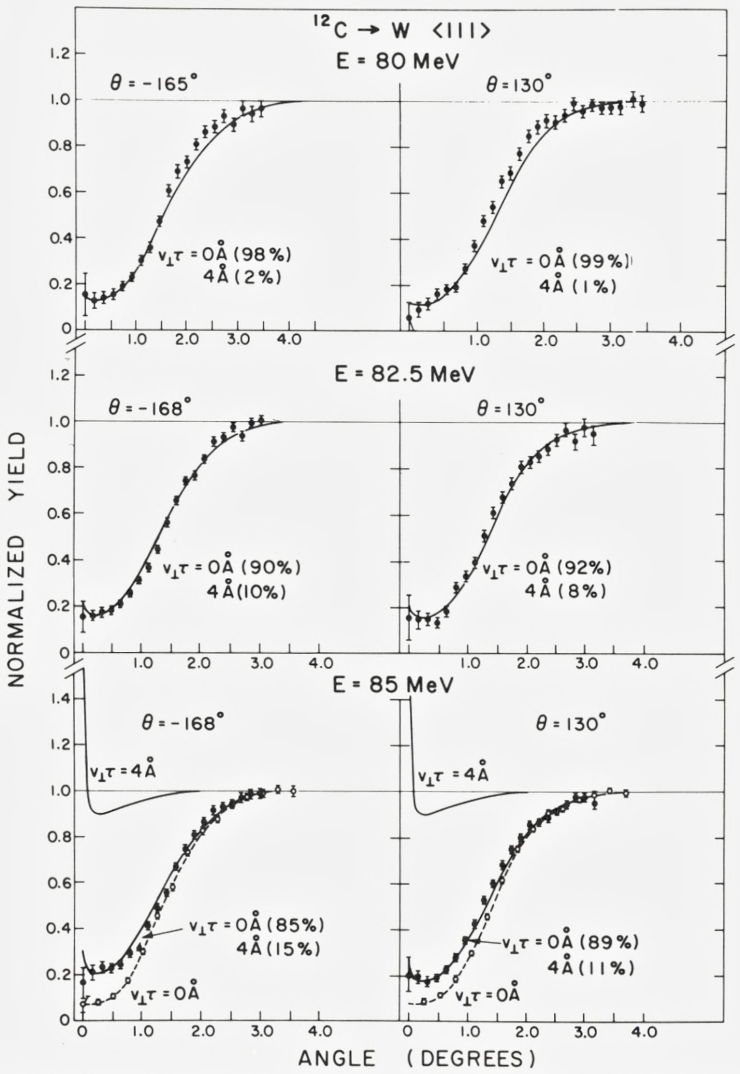

Fig. 15: Fission-fragment blocking dips for 80-, 82.5-, and 85-MeV ^{12}C bombardment of W for $\theta_R = 30°$. For 85-MeV, the short- and long-recoil dips used in the fits are also shown.

qualitative discussion in the introduction. Unfortunately, it was not possible to check the low-energy limit for ^{16}O projectiles. Close to the Coulomb barrier, the elastic, or quasi-elastic, large-angle scattering becomes very strong compared to the fission yield, and the fission fragments could not be separated from back-scattered oxygen. This separation is possible for ^{12}C projectiles (cf. fig. 5) because

Table 4. Results of two-component fits to W(^{12}C,f) data (see table 3).

E(MeV)	Det. Angle	$v_\perp\tau$(Å)	Amount χ_L(%)
80	−165°	4.0	1.8 ± 1.2
	130°	4.0	1.8 ± 2.0
82.5	−168°	4.0	9.1 ± 0.6
	130°	4.0	6.6 ± 1.2
85	−168°	4.0	15.0 ± 0.8
	130°	4.0	11.2 ± 0.6
87	−165°	4.0	14.5 ± 0.5

of the lower stopping power and the consequent lower value of the maximum energy deposited in the thin counters. The results of a series of measurements between 80 and 85 MeV are shown in fig. 15. The dips are again fitted by two components and the resulting magnitudes are given in table 4, which also includes one measurement at 87 MeV. It is seen that the long component increases with energy, being virtually zero at 80 MeV. Like the result for 115-MeV ^{16}O on tungsten, this is an important check of the validity of the analysis based on a comparison with scaled elastic dips. The energy dependence of the long component is consistent with the qualitative discussion in the introduction since in this energy region, the fission probability is small and increases rapidly with energy[32,34].

Only two short runs were made for ^{19}F bombardment of tungsten, one at 95 MeV and one at 108 MeV. Least-squares fits to the backward-counter ($\theta = -165°$) data gave long-lifetime components of 16 ± 8% ($v_\perp\tau = 1$ Å for 96 MeV and 10 ± 0.5% ($v_\perp\tau = 4$ Å) for 108 MeV. The statistical error for the 95-MeV point is large, but the results are in qualitative agreement with the energy dependence of the ^{16}O + W data (cf. fig. 16).

6. Discussion and Comparison with Calculations

6.1 *Qualitative Remarks*

Before making a comparison with detailed calculations, we examine the results on the basis of the simple qualitative picture described in the introduction. For this purpose, the magnitude of the long-lifetime component χ_L for fission induced by oxygen bombardment of tungsten is shown in fig. 16 as a function of bombarding energy. The decrease of χ_L at the highest bombarding energies was, as discussed in the introduction, expected because of the increase in fissionability at high angular momentum. Also, the increase in initial excitation energy of the com-

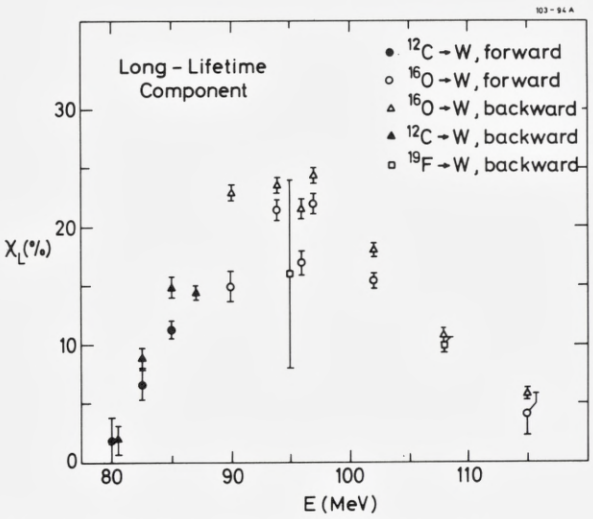

Fig. 16: The percentage of a long-lived component in the ^{12}C, ^{16}O, and ^{19}F-induced fission of W, as a function of projectile bombarding energy. The results have been obtained from two-component fits to the blocking dips measured at different detector angles (backward $\sim 165°$, forward 100° or 130°, cf. tables 3 and 4).

pound nucleus will in itself tend to reduce the importance of fission at low excitation energy, since the number of neutrons to be evaporated before fission increases.

The behaviour at low bombarding energy could not, for technical reasons, be studied for oxygen projectiles (cf. sec. 5.4). However, the measurements with carbon as projectile have been included in the figure, and these data confirm the predicted increase of χ_L, from an initally low value, with bombarding energy. Plotting the data against projectile bombarding energy is somewhat arbitrary. For a given bombarding energy, both the excitation energies (cf. table 5) and the angular-momentum distributions are rather different for the different compound nuclei, but for the present qualitative discussion, this is not so important.

Fig. 16 shows values of χ_L for both detector systems; there appears to be a systematic difference with the backward detector ($\theta \sim 165°$) having the larger value of χ_L. This effect will be discussed later together with the anisotropy of the fission-fragment angular distributions.

Table 5. Relative abundance of W isotopes and Q values for fusion with ^{12}C and ^{16}O.

Isotope of tungsten	Abundance (%)	Fusion Q Value	
		^{12}C	^{16}O
182	26.2	−16.0	−27.1
183	14.3	−15.3	−25.8
184	30.7	−13.8	−24.3
186	28.7	−11.5	−21.3

6.2 *Calculations*

It is only through a comparison with realistic calculations, such as those of Hagelund and Jensen[13], that the full information contained in the measurements is brought out. Considerable improvements have been made in the calculations, and details are given in the Appendix. Fig. 17 shows results for the fission and neutron-evaporation process for two ^{16}O bombarding energies. In the initially formed compound nucleus, ^{198}Pb, the excitation energy is well defined, and the top curve for both cases shows the contributions from different spin values to the total first-chance fission yield. These curves deviate from the triangular shape of the spin distribution due to the spin dependence of the fission probability, which is quite strong for the largest angular-momentum values.

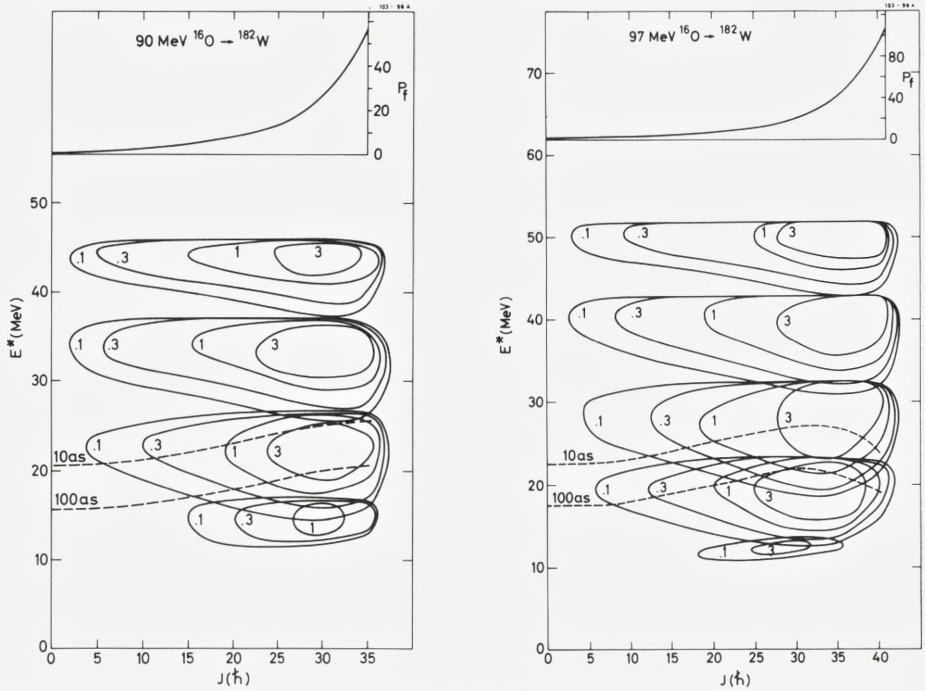

Fig. 17: Calculated contour diagrams of the population distribution, weighted with the fission probability, in excitation energy E* and spin J for 90- and 97-MeV ^{16}O-induced fission of ^{182}W. The curves centred at different excitation energy correspond to successive nuclei resulting from the nucleus after emission of one to five neutrons, i.e., with A = 197, 196, 195, 194, 193. The dashed lines are for constant lifetimes of 10 and 100 as for the isotopes A = 195 (90 MeV) and A = 194 (97 MeV). For the compund nucleus ^{198}Pb itself, the excitation energy is well defined, 55 MeV and 62 MeV for ^{16}O energy 90 MeV and 97 MeV, respectively, and the top curves show the fission probability as a function of spin, weighted by the triangular spin distribution. Values are in units of 10^{-4} $\hbar^{-1}$, and the numbers on the contours are in units of 10^{-4} $\hbar^{-1}$ MeV^{-1}.

For higher-chance fission, the distribution in excitation energy becomes increasingly broad owing to the spread in energy of evaporated neutrons. The fission contributions are indicated by contours of constant yield. The different stages contribute almost equally and fission at high spin values dominates.

The lifetime is determined mainly by the excitation energy. The dashed lines indicate contours of constant lifetime for the compound nucleus after evaporation of three and four neutrons, respectively, for 90- and 97-MeV bombarding energy. For the lowest spin values, neutron evaporation dominates, and the excitation energy for constant lifetime increases with increasing spin. For high-spin values, the fission width increases rapidly for fixed excitation energy, and therefore the dashed curves bend down as seen for the 97-MeV case. The two dashed curves divide the (E*,J) plane into three regions, corresponding approximately to short, intermediate, and long lifetimes ($v\tau \simeq 3$ Å for $\tau = 10^{-16}$ s). The calculations presented in fig. 17 indicate that for 90-MeV bombarding energy, the lifetime distribution will have a large component in the intermediate-lifetime region, while for 97 MeV, long-lifetime values will be strongly populated.

The choice of parameters used in the calculations is dicussed in detail in the Appendix. Here, we comment briefly on the constraints imposed by the three types of data.

(i) Total fission cross sections

If the cross section for complete fusion is known, a measured fission cross section may be converted into an effective fission probability P_f summed over all stages of fission, and this quantity depends sensitively on the magnitude of the fission barriers. The requirement that the calculations reproduce the measured fission cross sections for all ^{16}O bombarding energies for all tungsten isotopes is the main constraint on the absolute magnitude of the fission barrier and its variation with mass number. With the parameters given in the Appendix, all measured fission cross sections are reproduced within 10% (cf. tables A2 and A3).

(ii) Lifetime distributions

The importance of fission at the different stages of the evaporation chain depends on the relative magnitude of the corresponding fission barriers, and the long-lifetime component will thus be very sensitive to the A dependence of the fission barrier. This dependence is already constrained by the total cross sections, but when the mass is reduced by neutron evaporation, the excitation energy is also reduced, and the effective fission barrier may change due to the temperature dependence of shell corrections. The magnitude of such corrections and the manner in which they are included in the level density are therefore of special importance for the calculated lifetime distributions.

(iii) Fission-fragment angular distributions

The anisotropy of the fission-fragment angular distributions depends on the angular-momentum distribution, the effective moment of inertia at the barrier deformation, and the average temperature of the fissioning nuclei. The temperature is constrained by the lifetime measurements, the moments of inertia may be calculated as rigid-body values if the deformation at the barrier is known, and the measured anisotropy then sets narrow limits for the spin distribution of the fissioning nuclei. As mentioned above, this distribution is important for the analysis of the total cross-section measurements. In the interpretation of the lifetime measurements, it is necessary to take into account the large anisotropy in the angular distributions. This is discussed later in connection with the comparison of measured and calculated angular distributions of fission fragments.

6.3 *Lifetime Distributions*

Some calculated lifetime distributions are shown in figs. 18-20. In fig. 18 the variation of the lifetime distribution with bombarding energy is shown for the most important isotope, ^{182}W. In qualitative agreement with the measurements shown in fig. 16, the long-lifetime component ($\tau > 10^{-16}$ s) initially increases with increasing bombarding energy to a maximum $\chi_L \simeq 20\%$ between 90 and 100 MeV.

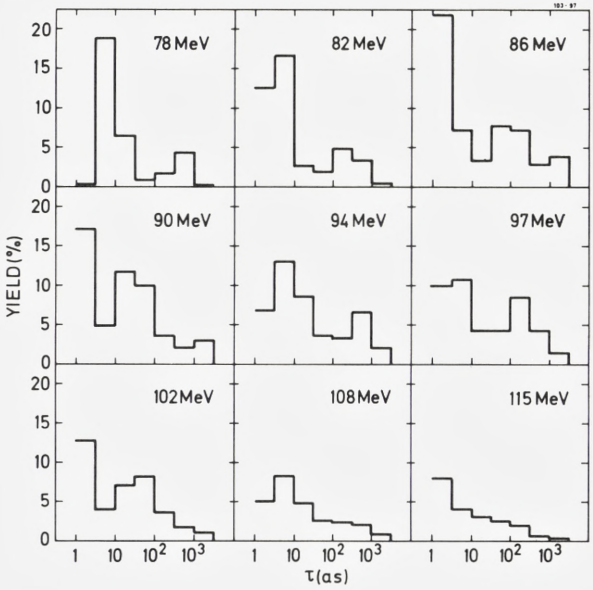

Fig. 18: The calculated percentage yield for ^{16}O-induced fission of ^{182}W as a function of lifetime τ for nine bombarding energies. The total yield for each bombarding energy is 100%, but only those components with $\tau > 1$ as are shown.

It is important to note that although the absolute magnitude of χ_L in the intermediate-energy region has been fitted by parameter adjustment to agree with experiment, this is not the case for the energy dependence of χ_L.

The distributions shown in fig. 18 have structure corresponding to the separation into the different stages of fission in the evaporation chain (cf. fig. 17). With increasing bombarding energy, the average lifetime for a particular stage decreases by about one order of magnitude per 10 MeV. The contribution from fission for A = 195 (fourth chance) moves from $\tau \sim 10^{-16} - 10^{-15}$ s at 78-82 MeV to $\tau \sim 10^{-17} - 10^{-16}$ s at 90 MeV and finally to short lifetimes, $\tau < 10^{-17}$ s, for 97 MeV and above. At the highest bombarding energies, there is little structure in the lifetime distributions since the energy distributions for the last stages of fission overlap strongly.

The lifetime measurements were made with tungsten targets of natural composition, and the results must be compared to a weighted sum of lifetime distri-

Fig. 19: Calculated yield as a function of lifetime for ^{16}O-induced fission of natural-composition W at 90-MeV bombarding energy. The weights assigned to the different isotopes have been obtained from the measured cross sections combined with the natural abundances.

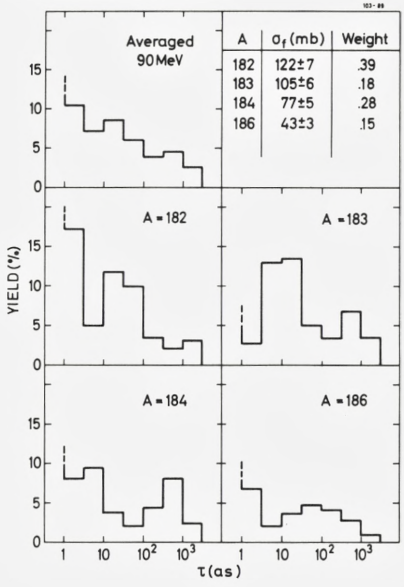

Fig. 20: Calculated yield, as a function of lifetime, for ^{16}O-induced fission of natural-composition W at 97-MeV bombarding energy (cf. caption to fig. 19).

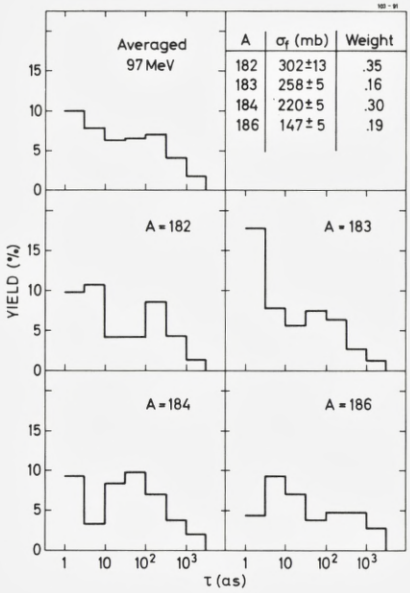

butions for the individual isotopes. The relative abundances and Q values for the different isotopes are given in table 5. Since the Q values are different for the different isotopes, the averaging smears most of the structure in the individual lifetime distributions. The results for 90- and 97-MeV bombarding energy are shown in figs. 19 and 20. There is little difference between these two lifetime distributions, but in qualitative agreement with experiment, the number of fissioning nuclei having lifetimes $\tau \simeq 10^{-17} - 10^{-16}$ s is slightly larger at 90 MeV.

Fission from long-lived, $\tau > 10^{-16}$ s, compound nuclei will contribute a long-recoil component for both the backward and the forward detectors. The projection factors ($\sin\theta$) for the two directions of observation differ by a factor 3-4, corresponding approximately to one interval in lifetime in figs. 18-20. The long-recoil components in the two directions should therefore differ by an amount approximately equal to the population of the interval $\tau = 3 \times 10^{-17} - 10^{-16}$ s, i.e., the long component χ_L should be larger by about 5% in the forward detector for the cases illustrated in figs. 19 and 20. As seen in table 3 and fig. 16, this is not the case. However, the apparent inconsistency may be explained by the large anisotropy of the fission-fragment angular distributions, as discussed below.

6.4 *Fission-Fragment Angular Distributions*

In the fission of high-spin compound nuclei created by heavy-ion bombardment, the fragment angular distribution is strongly anisotropic[33]. The reason for this is that, due to the large nuclear deformation at the fission barrier, the moment of inertia will be very different for rotations with angular momentum parallel and perpendicular to the axis of deformation; therefore, the rotational energy will depend on the relative orientation of the spin and the deformation axis. For an axially symmetric deformation, one may denote the two moments of inertia by $\mathfrak{I}_{\parallel}$ and $\mathfrak{I}_{\perp}$ and introduce an effective moment of inertia by $1/\mathfrak{I}_e = 1/\mathfrak{I}_{\parallel} - 1/\mathfrak{I}_{\perp}$. The decisive parameter is the ratio of the difference in rotational energy to the nuclear temperature [33], $2p = \hbar^2 I(I+1)/(2T\mathfrak{I}_e)$ where $I\hbar$ is the angular momentum. When p is large, the fragments will be emitted preferentially in the plane perpendicular to the angular-momentum vector. For a compound nucleus created by ion bombardment, the spin is perpendicular to the beam direction, and confinement of the fission fragments to the plane perpendicular to the spin direction corresponds to an angular distribution proportional to $1/\sin\theta$, where θ is the angle relative to the beam direction. For finite values of p, the angular distribution will deviate from $1/\sin\theta$ at angles close to 0° and 180° and reach a maximum depending on the parameter p. A measurement of the anisotropy therefore determines the effective value of p.

The main problem in the analysis is usually that all three quantities in the

expression for p, i.e., I, $\mathfrak{J}_e$, and T, are uncertain. In the present case, there is independent information on the effective temperature from the lifetime measurements since the main uncertainty is associated with the fission distribution over several stages in the evaporation cascade. The effective moment of inertia may be calculated from rigid-body values if the nuclear deformation at the barrier is known. In the present calculations, we have chosen the value corresponding to the liquid-drop barrier. It is shown in the Appendix that it is possible to reproduce the measured anisotropies as well as the total fission cross sections with values of the maximum compound-nucleus spin which are consistent with the theoretical estimates of Bass[35]. A comparison of measured anisotropies and predictions for

Fig. 21: Angular distributions of fission fragments for 90-, 94-, and 97-MeV ^{16}O bombardment of ^{182}W, normalized to a $(\sin\theta)^{-1}$ distribution at 140° in the centre-of-mass system. The solid lines are calculated angular distributions, summed over all stages of fission.

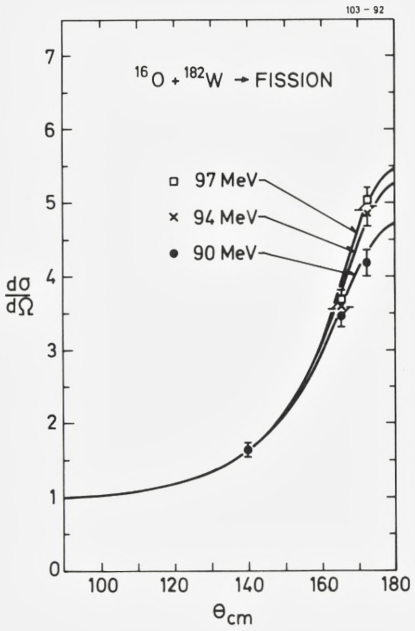

Fig. 22: Calculated fission-fragment angular distributions for 90-MeV ^{16}O bombardment of ^{182}W. The fission yield has been divided into three lifetime regions corresponding approximately to the short-, intermediate-, and long-lifetime regions of sensitivity in the blocking lifetime measurements. The dashed curve is the average angular distribution obtained by adding the contributions from all lifetimes.

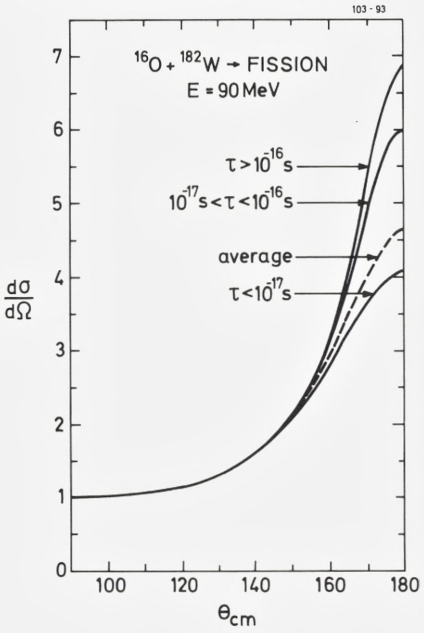

the isotope ^{182}W for ^{16}O bombarding energies of 90, 94, and 97 MeV is shown in fig. 21, and the comparison between all data and predicted values is given in table A4 in the Appendix.

The curves in fig. 21 represent weighted averages over all stages of fission and thus over a broad range of temperatures. The early-stage fission at high temperature is less anisotropic than late-stage fission at lower temperature. Since the nuclear lifetime varies rapidly with the nuclear temperature, the anisotropy and the lifetime will be strongly correlated. This is shown in fig. 22 for 90-MeV ^{16}O on ^{182}W. The fission yield has been divided into three lifetime regions, and the angular dependence of the cross section is given for each interval separately as well as for the total. At backward angles, the intermediate- and long-lifetime components are enhanced relative to the average by 25-30%. This offers an explanation for the difference between the χ_L values for the forward and backward counters which is observed (cf. fig. 16) when the analysis is made with average recoil distances for the long component consistent with the difference in projection factor.

7. Concluding Remarks

We believe that the present systematic measurements demonstrate that a new type of analysis must be adopted in the application of the blocking technique to lifetime measurements of heavy-ion-induced fission. Lifetimes cannot be extracted from the difference $\Delta\chi$ of minimum yields for blocking patterns recorded at different angles to the incident beam. An analysis in terms of several components with different lifetimes, however, can yield useful information. We have limited ourselves to two components in the present analysis, but in some cases, more information may be obtained by including a third component [34] or by introducing a continuous lifetime distribution characterized by a few parameters.

Our results, particularly for the energy dependence of the long-lifetime component, are consistent with expectations based on a simple physical picture of the fission process. It has also been possible to reproduce the data by detailed numerical calculations, including the full neutron-evaporation cascade. In this regard, it was important to combine the lifetime results with measurements of total fission cross sections and fission-fragment angular distributions. Although the set of parameters in the calculations, which reproduces the available data, is not unique, the ambiguities are greatly reduced compared to cases where only one type of data, such as total cross sections, is analyzed. In particular, the new information obtained from the lifetime measurements appears to be very useful.

We intend to continue the experiments with monoisotopic tungsten crystals. Such measurements should add further parameter constraints to the calculations, and we hope also to obtain more detailed information on the time distributions when the results are not smeared by an average over isotopes.

Acknowledgements
We would like to thank our collegues for many stimulating discussions in connection with the present research project. Of particular value were several discussions with W. J. Swiatecki. We also want to acknowledge the excellent technical assistance, both at the Chalk River Laboratories and at the Physics Institute, University of Aarhus. The Danish participation in the collaboration was made possible by funds from the Danish Committee for Accelerator Physics.

APPENDIX

The main features of the theoretical model were described in ref. 13, where it was shown that calculations based on this model qualitatively reproduce the experimental findings. We have extended the calculations with the more ambitious goal of reproducing quantitatively the experimental data, which have been supplemented with measurements of fission-fragment angular distributions. For this purpose, some improvements to the model have been introduced, and in the following discussion we shall indicate these modifications.

The first part of the appendix is a broad outline of the theoretical model used, with expressions for the most important quantities. In the second part is discussed how the parameters are determined and which of them are most important for reproducing the present data. The third part contains the results of the model calculations and a comparison with the experimental values.

A1. Theoretical Model

The fission process is assumed to proceed via the formation of a compound nucleus with a well-defined excitation energy and a spin distribution characterized by a sharp cut-off at a maximum angular momentum I_m. Three modes of decay are included, viz. fission, neutron emission, and γ emission, and the development of the distribution in excitation energy and spin of the nucleus is followed through the neutron-evaporation cascade.

A1.1 *Widths*

The partial widths for the three decay modes are calculated from the standard formulas for a statistical model, which express the widths in terms of level densities and appropriate constants and weighting functions. The neutron width may be expressed as a sum of contributions from final nuclear states with spin I' and excitation energy $E - B_n - \varepsilon$,

$$\Gamma_n(E,I) = \sum_{I'} \int_0^{E-B_n} \Gamma_n(E,I,\varepsilon,I')\,d\varepsilon, \tag{A1}$$

with

$$\Gamma_n(E,I,\varepsilon,I') = \frac{1}{2\pi\varrho_C(E,I)} \sum_{j=|I-I'|}^{I+I'} \sum_{\ell=|j-\frac{1}{2}|}^{j+\frac{1}{2}} \varrho_D(E-B_n-\varepsilon,I')\,T_{\ell j}(\varepsilon), \tag{A2}$$

where ϱ_C and ϱ_D are the level densities for the nucleus before and after the neutron emission and $T_{\ell j}(\varepsilon)$ are the neutron-transmission coefficients for orbital angular momentum ℓ, total spin j, and kinetic energy ε.

The fission width is given by

$$\Gamma_f(E,I) = \frac{1}{2\pi\varrho_C(E,I)} \int_0^E \frac{\varrho_B(\varepsilon,I)\,d\varepsilon}{1+\exp\left(-\frac{2\pi}{\hbar\omega}(E-B_f-\varepsilon)\right)}, \tag{A3}$$

which for $E > B_f$ reduces to

$$\Gamma_f(E,I) \simeq \frac{1}{2\pi\varrho_C(E,I)} \int_0^{E-B_f} \varrho_B(\varepsilon,I)\,d\varepsilon\,. \tag{A4}$$

Here ϱ_B is the level density at the saddle point for fission. Note that the dependence of the effective fission barrier on angular momentum is implicity included through this level density (cf. eq. A8). The main parameter in eq. (A3) is the fission barrier B_f. It may be expressed as a smooth contribution $\tilde{B}_f$ corrected for barrier and ground-state shell and pairing corrections,

$$B_f = \tilde{B}_f - \delta U_{gs} - \delta P_{gs} + \delta U_B + \delta P_B\,. \tag{A5}$$

The radiation width is given by

$$\Gamma_\gamma(E,I) = \frac{1}{2\pi\varrho_C(E,I)} \sum_{J=|I-1|}^{I+1} \int_0^E \varrho_C(E-\varepsilon,J) f(\varepsilon)\,d\varepsilon\,. \tag{A6}$$

In contrast to ref. 13, we have used a function $f(\varepsilon)$ given by the giant dipole expression [36a],

$$f(\varepsilon) = c_\gamma \frac{8}{3} \frac{1.4}{mc^2} \frac{e^2}{\hbar c} \frac{NZ}{A} \frac{\Gamma_G \varepsilon^4}{(\Gamma_G\varepsilon)^2 + (\varepsilon^2 - E_G^2)^2} \tag{A7}$$

The fraction of exchange force present in the nuclear force is taken as 0.5 as in ref. 37, leading to the value 1.4 in eq. (A7).

A1.2 *The level density*

The intrinsic level density $\varrho(E)$ is taken from ref. 15 for energies larger than the largest critical energy for disappearance of pairing. For smaller energies, a smoothly connected constant-temperature expression ($\varrho(E) \propto \exp(E/T)$) is used. With this assumption, the number of levels at zero excitation energy agrees reasonably well with experiments.

A spin dependence of the shell correction (as introduced in ref. 13) is not included because of its small effect and the uncertainties and complications involved.

The total level density is obtained as usual for an axial- and R-symmetric system by assuming a rotational band built on top of each intrinsic level[38], leading to

$$\varrho(E,I) = \frac{1}{2\sqrt{2\pi \mathfrak{J}_{\parallel} T}} \sum_{K=-I}^{I} \varrho\left(E - \frac{I(I+1)}{2\mathfrak{J}_{\perp}} - \frac{K^2}{2\mathfrak{J}_e}\right). \tag{A8}$$

When the rotational energies are small relative to E, this simplifies to

$$\varrho(E,I) \simeq \frac{\varrho(E)}{2\sqrt{2\pi \mathfrak{J}_{\parallel} T}} \exp\left(-\frac{I(I+1)}{2\mathfrak{J}_{\perp} T}\right) \sum_{K=-I}^{I} \exp\left(-\frac{K^2}{2\mathfrak{J}_e T}\right). \tag{A9}$$

Here, $\mathfrak{J}_{\parallel}$ and $\mathfrak{J}_{\perp}$ denote the moments of inertia parallel and perpendicular to the symmetry axis, and $\mathfrak{J}_e$ is the effective moment of inertia, $1/\mathfrak{J}_e = 1/\mathfrak{J}_{\parallel} - 1/\mathfrak{J}_{\perp}$. The temperature T is given by

$$1/T = \frac{\partial}{\partial E} \ln \varrho(E) . \tag{A10}$$

This level density is used both at the ground-state and barrier deformations. At first it may seem strange to count rotational levels at the ground state of, e.g., ^{200}Pb, which is usually assumed spherical. The argument is that fairly high spin states (25ħ-50ħ) are populated, leading to a deformed equilibrium shape. Furthermore, even for low spin values, the nucleus has a finite probability of being deformed. Since the rotational enchancement factor is very large, it is conceivable that a flat, spherical equilibrium effectively requires a level density including rotational contributions. Attempts to analyze cross sections for fission of spherical nuclei induced by light particles indicate that such a level density should always be used. This is the case even for high excitation energies ($\gtrsim 50$ MeV) where the rotations are usually expected to vanish for ground-state deformations [38].

A1.3 *Moments of inertia*

The moments of inertia have rigid-body values as expected[39] for high excitation energy, high spin, and large deformation. They are calculated from a uniform distribution with a sharp cut-off at the boundary. The shape is axially symmetric around the z axis and given by[40]

$$\varrho^2 = (c^2R^2 - z^2)(A + Bz^2/(c^2R^2)) , \tag{A11}$$

$$\frac{1}{c^3} = A + \frac{1}{5}B\,, \quad B = \frac{1}{2}(c-1) + 2h\,, \quad R = r_0 A^{1/3}\,, \tag{A12}$$

where c and h are deformation parameters. The moments of inertia are then for a system of N nucleons

$$\mathfrak{J}_{\parallel} = \frac{2}{5} mNR^2 c^5 \left\{ \frac{B^2}{21} + A^2 + \frac{2}{7} A \cdot B \right\}, \tag{A13}$$

$$\mathfrak{J}_{\perp} = \frac{1}{5} mNR^2 c^5 \left\{ A + \frac{3}{7} B \right\} + \frac{1}{2} \mathfrak{J}_{\parallel}\,. \tag{A14}$$

A1.4 *Angular distribution of fission fragments*

For a nucleus of spin I and energy E, the distribution of the emitted fission fragments with respect to the beam axis is approximately[33,41]

$$W_{E,I}(\theta) = \sqrt{\frac{2p}{\pi}} \frac{J_0(ip\sin^2\theta)\exp(-p\sin^2\theta)}{\mathrm{erf}(\sqrt{2p})}, \tag{A15}$$

where

$$p = \frac{(I+\frac{1}{2})^2}{4K_0^2}\,, \quad K_0^2 = T_B \mathfrak{J}_e(\mathrm{Barrier})\,. \tag{A16}$$

Here erf is the error function and J_0 the zero-order Bessel function. The temperature T_B corresponds to the intrinsic excitation energy at the barrier and therefore depends on spin,

$$\frac{1}{T_B} = \frac{\partial}{\partial E} \ln \varrho_B(E - B_f, I)\,. \tag{A17}$$

Expression (A15) corresponds to the relative probabilities of different projections K of the spin on the symmetry axis, which are implicitly given in eq. (A8). However, to arrive at eq. (A15), only the expansion in the last parameter in eq. (A8), $K^2/2\mathfrak{J}_e$, is necessary. The total angular distribution $W(\theta)$ is obtained by summing and integrating eq. (A15) over the spin and energy distribution P(E,I) of all stages in the evaporation cascade, weighted, of course, with the fission probability,

$$W(\theta) = \sum_{\text{Nuclei}} \sum_{I} \int dE\; P(E,I) \frac{\Gamma_f(E,I)}{\Gamma_{\text{total}}(E,I)} W_{E,I}(\theta)\,. \tag{A18}$$

A2. Parameter Determination for $^{16}O + W$

The parameters fall into two groups. One consists of parameters either fixed from independent considerations or relatively unimportant for the present data; these are discussed in the first two sections. The second group contains the parameters crucial for the present data, i.e., those about which the present experiments give information. They are discussed in the last three sections.

A2.1 *Neutron- and gamma-width parameters*

The neutron transmission coefficients are obtained from an optical model with the average parameter set recommended in ref. 42 for lower energies. They are fixed from the beginning, and no readjustment or search for better parameters has been attempted.

The giant dipole parameters in eq. (A7) are [43]

$$\Gamma_G = 5 \text{ MeV}, \quad E_G = \frac{80 \text{ MeV}}{A^{1/3}}, \quad c_\gamma = 2. \tag{A19}$$

With this choice for c_γ, we find Γ_γ values roughly in agreement with the observed average gamma width [36b] at the neutron-binding energy for nuclei below the closed shell of ^{208}Pb. Gamma emission is competitive only for the lowest excitation energies, but the magnitude of Γ_γ is important for the contribution to the fission yield from very long lifetimes, i.e., for the magnitude of the long-lifetime component.

A2.2 *General level-density parameters*

The level-density parameters[15] consist of the main parameter a, the parameter κ, the two pairing gaps Δ_n and Δ_p, the shell distance $\hbar\omega$, the shell correction δU, and the moments of inertia. For a and $\hbar\omega$, we have used the values of ref. 15, and since κ enters (weakly) only at small excitation energies, we chose $\kappa = 0.0$.

The gap parameters appear only through the critical energies and the pairing energies; we used the same set (different for the ground states and the barriers) for all nuclei. This choice, with the values selected for the other parameters, gives an average distance of D = 27 eV between $\frac{1}{2}^+$ levels in $^{195}_{82}$Pb at an excitation energy of 6.3 MeV, in agreement with the corresponding observed quantity for the nearby nucleus $^{193}_{78}$Pt. The values of a, κ, $\hbar\omega$, and Δ are:

$$\begin{aligned} &a = A/9.5 \text{ MeV}, \quad \hbar\omega = 41 \text{ MeV}/A^{1/3}, \quad \kappa = 0.0 \\ &\Delta_n^{gs} = \Delta_n^B = \Delta_p^B = 0.8 \text{ MeV}, \quad \Delta_p^{gs} = 0.5 \text{ MeV} \end{aligned} \tag{A20}$$

A2.3 *Shell corrections*

The shell-correction term is important for the energy dependence of the level density, and many prescriptions are available. We have taken δU of ref. 44 for the ground-state shell correction. It increases with the distance from the closed neutron shell N = 126 until N = 113 (A = 195), after which it stays constant at about −2 MeV. Instead of this constant value, we continued the increase by adding 0.1 MeV for A = 195, 0.2 MeV for A= 194, 0.3 MeV for A= 193, etc. This has little effect on our numerical level-density results because δU in the level density is multiplied by a small factor for small excitation energies where these nuclei play a role. However, since we use a constant smooth part $\tilde{B}_f$ of the fission barrier (see eq. A5 and A21), such a modification implies that the barriers B_f have to be decreased by the same amount, which has the important effect of increasing the long-lifetime component for the two lightest tungsten isotopes.

The barrier shell correction is presumably less dependent on nucleon number, and we have simply used a constant value $\delta U_B = -2$ MeV. It enters the barrier level density as an energy shift which, for large excitation energies, amounts to δU_B (in this case decreasing the number of levels on top of the barrier) and for small excitations approaches zero. Decreasing δU_B therefore has the effect of decreasing the fission probability at high excitation energy while leaving the fission probability at low excitation energy essentially unchanged. This means a relative increase of the late-stage fission (long-lifetime component). Thus δU_B is a very selective parameter for shifting the relative fission contribution from short to long lifetime or vice versa. Some support for the value chosen for δU_B may be found in ref. 45.

A2.4 *The smooth part of the fission barrier*

The fission barrier is obtained from eq. (A5). The shell corrections were discussed in sec. A2.3 and the pairing corrections[15] are obtained from the paring gaps*) in eq. (A20). Thus only the smooth barrier term $\tilde{B}_f$ is left to be specified. For the application described here we required a constant value (independent of A) of B_f and the experimental fission cross sections were reproduced with

$$\tilde{B}_f = 11.3 \text{ MeV}. \qquad \text{(A21)}$$

Inclusion of the pairing corrections (see eq. (A5)) in the smooth barrier reduces the value in eq. (A21) to 10.5 MeV. This may be compared to the droplet-model result [46] of 13.9 MeV. An analysis of fission cross sections similar to ours has been

*) In ref. 15, a factor $6/\pi^2$ was inadvertently omitted on the right-hand side of eq. (A24). The quantity A in this equation is the number of protons or neutrons.

published by Ignatyuk et al. [47]. Their results for the smooth barrier are smaller than the droplet-model values by approximately the same amount, e.g., 3.0 MeV for ^{200}Hg.

A2.5 *Spin distribution and moments of inertia*

The parameters in the expressions for the moments of inertia are c, h, and r_0. For the radius parameter, we take the same value for all nuclei regardless of deformation. The ground-state shape is assumed spherical. This choice is natural for the lead isotopes although we assumed rotational contributions in the corresponding level density. The ground-state moments of inertia enter only weakly in the fission probability and lifetime distribution, and the actual deformation used is therefore not critical.

For the barrier deformation we assumed the liquid-drop value, which is expected[48] for high excitation energy where the shell effects have disappeared. For low excitation energy, the shell effects should be included in the determination of the barrier deformation. However, for the lead isotopes in question, the barrier (in deformation space) is broad and relatively flat[40], and consequently, one may expect that the liquid-drop value is approached relatively quickly with increasing energy.

The values assumed were

$$\begin{aligned} &r_0 = 1.2 \text{ fm}, \quad (c,h)_{gs} = (1.0, 0.0)\,, \\ &(c,h)_B = (1.87, 0.0) \end{aligned} \tag{A22}$$

The spin distribution in the initial compound nucleus is assumed proportional to $2I+1$ with a sharp cut-off at the maximum value I_m. It is related to the complete-fusion cross section by

$$\sigma_{CF} = \pi \lambda\!\!\!^{-2} (I_m + 1)^2\,, \tag{A23}$$

where $\lambda\!\!\!^{-}$ is the de Broglie wavelength for the reduced mass and centre-of-mass energy. The Bass model[35] gives similar expressions for the complete-fusion and the total-reaction cross section with corresponding maximum spin values I^B_{CF} and I^B_R.

The experimental fission probability P_f is determined as $P_f = \sigma_f/\sigma_{CF}$, where σ_f is the measured fission cross section and σ_{CF} is given by eq. (A23). The quantity I_m thus enters both in observed and in calculated quantities. The value of I_m is especially important for the fission-fragment anisotropy (see eqs. (A15) and (A16)), but it also has a significant effect on both the calculated and the observed fission

probabilities. With the parameter set described above, I_m is chosen for each projectile energy to obtain agreement between experiment and calculation. The resulting I_m values lie between I^B_{CF} and I^B_R, determined from the Bass model.

A barrier deformation smaller than that in eq. (A22) leads to a larger $\mathfrak{I}_e$ value which, in turn, requires a larger I_m to reproduce the fission-fragment anisotropy. For example, with $c_{B_i} = 1.5$, corresponding to the low-energy barrier with shell effects included, $\mathfrak{I}_e$ is increased by a factor of 1.7 which, for the case of 97 MeV $^{16}O + ^{182}W \rightarrow ^{198}Pb$ requires $I_{m_i} = 52\hbar$, i.e., 50% larger than the Bass value. For the same case, the barrier in eq. (A22) leads to a value 14% higher than I^B_{CF}. Thus, if I_m is assumed close to the value obtained in the Bass model, the effective moment of inertia determined from experiment is that corresponding to the liquid-drop deformation.

A3. Results

A.3.1 $^{16}O + W$

Table A1 gives the input parameters used in the calculations together with other quantities of interest. This parameter set reproduces the measured fission-fragment anistotropy and fission probability and leads to a lifetime distribution consistent with what is observed. The main parameters are the smooth part of

Table A1. Statistical model parameters as functions of mass number A for the Pb isotopes in the calculations. The neutron binding energy B_n, fission barrier B_f, shell and pairing corrections δU and δP, for the ground state (gs) and the barrier (B), and the critical energy E^c, are given in MeV. The moments of inertia for the ground state and barrier deformations are given in units of $\hbar^2$/MeV.

A	B_n	B_f	δU_{gs}	δP_{gs}	δP_B	E^c_{gs}	E^c_B	$\mathfrak{I}^{gs}$	$\mathfrak{I}^B_{\|\|}$	$\mathfrak{I}^B_{\perp}$	$\mathfrak{I}^B_e$
202	8.70	14.0	−5.56	−2.53	−3.36	6.4	7.2	96.5	47.6	302.3	56.5
201	7.20	13.4	−5.00	−1.71	−2.54	4.0	7.2	95.7	47.2	299.8	56.0
200	9.10	12.8	−4.38	−2.49	−3.33	6.3	7.1	94.9	46.8	297.3	55.5
199	7.40	12.1	−3.73	−1.68	−2.51	3.9	7.1	94.1	46.4	294.8	55.1
198	9.44	11.6	−3.17	−2.46	−3.29	6.2	7.0	93.4	46.0	292.4	54.6
197	7.68	11.1	−2.66	−1.64	−2.48	3.8	7.0	92.6	45.6	289.9	54.1
196	9.75	10.7	−2.25	−2.43	−3.26	6.1	7.0	91.8	45.2	287.5	53.6
195	7.95	10.4	−1.95	−1.61	−2.44	3.7	6.9	91.0	44.9	285.0	53.3
194	9.95	10.2	−1.83	−2.39	−3.23	6.1	6.9	90.2	44.5	282.6	52.8
193	8.13	10.1	−1.73	−1.58	−2.41	3.7	6.9	89.5	44.1	280.2	52.3
192	10.14	10.1	−1.66	−2.36	−3.19	6.0	6.8	88.7	43.7	277.8	51.9
191	8.35	10.0	−1.59	−1.54	−2.38	3.6	6.8	87.9	43.3	275.4	51.4

the fission barrier $\tilde{B}_f$, the barrier shell correction δU_B, and the maximum spin I_m of the initial compound nucleus. Equally important but not varied are δU_{gs} and the effective moment of inertia at the barrier deformation.

Table A2. The maximum spin values I_R^B and I_{CF}^B, corresponding to the reaction and complete-fusion cross sections in the Bass model, are given for the reaction $^{16}O + ^{182}W \rightarrow {}^{198}Pb$. Also given are the maximum spin values I_m used in the calculations, the related complete-fusion cross sections σ_{CF}(mb), the measured fission cross sections σ_f(mb), and experimental (P_f^{exp}) and calculated (P_f^{calc}) fission probabilities. All quantities are given as functions of ^{16}O bombarding energy (MeV).

$E_{^{16}O}$	I_R^B	I_{CF}^B	I_m	σ_{CF}	σ_f	P_f^{exp}	P_f^{calc}
90	34.4	28.2	34	656	122	0.19	0.19
94	38.9	32.3	38	779	216	0.28	0.30
97	42.0	35.0	40	836	302	0.36	0.37
102	46.7	39.1	43	914	429	0.47	0.47
108	51.9	43.4	47	1027	571	0.56	0.56
115	57.3	47.8	50	1089			0.62

In table A2 we compare I_m to the Bass-model prediction as a function of energy. We note the smooth transition from the total-reaction value at low energy towards the complete-fusion value at high energy. These I_m values are also used for the other three tungsten isotopes. Table A2 also gives experimental and calculated fission probabilities, which differ at most by 7%.

Table A3. Experimental and calculated fission probabilities for the naturally occurring tungsten isotopes, for ^{16}O bombarding energies of 90 MeV and 97 MeV.

$E_{^{16}O}$		^{182}W	^{183}W	^{184}W	^{186}W
90	Calc.	0.19	0.17	0.11	0.066
	Exp.	0.19	0.16	0.12	0.066
97	Calc.	0.37	0.34	0.28	0.18
	Exp.	0.36	0.31	0.26	0.18

In table A3 is given the isotope dependence of experimental and calculated fission probabilities for bombardment with ^{16}O at 90 and 97 MeV. The agreement is within 10%. The fission-fragment anisotropy is given in table A4 for the different isotopes, and again the calculations reproduce the experimental results to within $\sim 10\%$.

Table A4. Experimental and calculated fission-fragment angular distributions in the centre-of-mass system, as functions of bombarding energy (MeV) for ^{16}O induced fission of the four W isotopes. The experimental distributions are normalized at $\theta_{cm} = 113°$ to a $(\sin\theta)^{-1}$ distribution and the calculated distributions are normalized to unity at $\theta_{cm} = 90°$.

Experiment

	A = 182		A = 183		A = 184		A = 186	
E	140°	172°	140°	172°	140°	172°	140°	172°
90	1.67	4.16	1.62	4.17	1.72	4.20	1.78	4.30
94	1.62	4.64	1.66	4.59	1.63	4.69	1.76	4.40
97	1.56	4.61	1.70	4.73	1.64	4.64	1.70	4.77
102	1.58	4.51	1.72	4.94	1.59	4.71	1.69	5.05
108	1.65	4.88	1.61	4.91	1.72	4.81	1.55	4.83

Calculation

	A = 182		A = 183		A = 184		A = 186	
E	170°	180°	170°	180°	170°	180°	170°	180°
90	4.10	4.72	4.19	4.87	4.04	4.66	3.82	4.36
94	4.46	5.25	4.55	5.39	4.53	5.41	4.41	5.23
97	4.57	5.43	4.63	5.52	4.66	5.60	4.61	5.54
102	4.65	5.52	4.70	5.61	4.75	5.71	4.77	5.77
108	4.71	5.59	4.78	5.71	4.81	5.78	4.88	5.92
115	4.70	5.58						

The lifetime distribution can be compared to experiment only for an average over isotopes. As discussed in the main text the distributions are consistent with experiment. The calculated energy dependence confirms the prediction from qualitative arguments discussed in the introduction and in sec. 6.1.

A3.2 $^{12}C + W$

The procedure described in sect. A2 was repeated for the reaction $^{12}C + W \rightarrow Hg$. The resulting parameter set was given and discussed in detail in ref. 34. The smooth part of the barrier, $\tilde{B}_f$, was first assumed constant as for the ^{16}O projectile, but a weak linear dependence on A turned out to be necessary for a good fit to the data.

The ground-state shell corrections were obtained from those for the Pb isotopes by adding 0.17 MeV due to the difference in proton number. This is 1 MeV less than expected from ref. 44. The barrier shell correction is $\delta U_B = -1.0$ MeV less negative than for the Pb isotopes.

The value of I_m, which changes with bombarding energy, was determined from the angular distribution. As for $^{16}O + W$, we found a transition from the complete-fusion value of Bass[35] at higher energies towards the total-reaction value at lower energies. The other parameters were determined as described in sect. A2 for the Pb isotopes.

A3.3 *Conclusions*

The main conclusion we can draw from these results is that the model parameters can be adjusted to reproduce the present heavy-ion data, i.e. the isotope and energy dependence of the fission probability, the anisotropy of the angular distribution and the isotope-averaged lifetime distribution.

The parameters are not unique, i.e., other sets exist which will also reproduce the data. There are two main degrees of freedom in the important set of parameters. The lifetime distribution depends only on the difference between shell corrections at the ground state and at the barrier, not on each one separately. Furthermore, with an average temperature fixed by the lifetime distribution, the anisotropy depends only on the ratio between the square of the maximum angular momentum and the effective barrier moment of inertia. We have not explored these and other degrees of freedom systematically, but it is clear that the requirement of reproducing the three different types of measurements simultaneously, for different isotopes and bombarding energies, sets narrow limits on the model parameters.

In some cases particle induced fission data for the same compound nuclei are available. Although our model can easily reproduce such data it is very difficult, if not impossible, to reproduce both sets of data with the same model parameters. As an example, one of the compound nuclei created by ^{12}C bombardment of tungsten, ^{198}Hg, has been studied also through proton induced fission of gold, and the results have been used[49] to extract the magnitude of the fission barrier for ^{198}Hg. The value obtained for B_f is about 5 MeV higher than the value found in ref. 34. One possibility is that the large negative ground-state shell corrections are strongly reduced for the high-spin states populated by heavy-ion bombardment. This explanation was suggested in ref. 34 and further support for it may be found in ref. 50.

References

1. W. M. Gibson, Ann. Rev. Nucl. Sci. *25* (1975) 465.
2. S. A. Karamyan, Yu. V. Melikov, and A. F. Tulinov, Fiz. El. Chast. Atom. Yad. *4* (1973) 456; Sov. J. Particles Nucl. *4* (1973) 196.
3. F. Brown, D. A. Marsden, and R. D. Werner, Phys. Rev. Lett. *20* (1968) 1449.
4. W. M. Gibson and K. O. Nielsen, Int. Symp. Phys. Chem. Fission SM122/129 (1969 IAEA: Vienna 861 pp.); Phys. Rev. Lett. *24* (1970) 114.
5. Yu. V. Melikov, Yu. D. Oststavnov, and A. F. Tulinov, Zh. Eksp. Teor. Fiz. *56* (1969); Sov. Phys. JETP *29* (1969) 968; Yad. Fiz. *12* (1970) 50; Sov. J. Nucl. Phys. *12* (1971) 27.
6. Yu. V. Melikov, Yu. D. Oststavnov, A. F. Tulinov, and N. G. Chechenin, Nucl. Phys. *A180* (1972) 241.
7. J. U. Andersen, K. O. Nielsen, J. Skak-Nielsen, R. Hellborg, and K. G. Prasad, Nucl. Phys. *A241* (1975) 327.
8. P. E. Vorotnikov, Yu. F. Gurtovenko, E. Kh. Kisina, V. O. Kordynkevitch, Yu. V. Melikov, N. A. Morogov, Yu. D. Oststavnov, L. N. Syutkina, A. F. Tulinov, and N. G. Chechenin, Nucl. Phys. *A281* (1977) 295.
9. J. U. Andersen, N. G. Chechenin, A. S. Jensen, K. Jørgensen, and E. Lægsgaard, Nucl. Phys. *A324* (1979) 39.
10. S. A. Karamyan, Yu. V. Melikov, F. Normuratnov, O. Otgonsuren, and G. M. Solovyeeva, Yad. Fiz. *13* (1970) 944; Sov. J. Nucl. Phys. *13* (1971) 543.
11. S. A. Karamyan, Yu. Ts. Oganesyan, and F. Normuratnov, Yad. Fiz. *14* (1971) 499; Sov. J. Nucl. Phys. *14* (1972) 279.
12. J. U. Andersen, E. Lægsgaard, K. O. Nielsen, W. M. Gibson, J. S. Forster, I. V. Mitchell, and D. Ward, Phys. Rev. Lett. *36* (1976) 1539.
13. H. Hagelund and A. S. Jensen, Physica Scripta *15* (1977) 225.
14. A. S. Jensen, *Proc. IAEA Int. Conf. on Neutron Physics and Nuclear Data for Reactors*, Harwell, U. K., Sept., 1978.
15. A. S. Jensen and J. Sandberg, Physica Scripta *17* (1978) 107.
16. H. C. Britt and A. R. Quinton, Phys. Rev. *120* (1960) 1768.
17. R. Vandenbosch and J. R. Huizenga, *Nuclear Fission* (Academic, New York, 1973) p. 234.
18. E. Lægsgaard, Nucl. Instrum. Methods *162* (1979) 93.
19. T. Sikkeland, Phys. Rev. *135* (1964) B669.
20. J. H. Barrett, Phys. Rev. *133* (1971) 1527.
21. J. Lindhard, K. Dan. Vidensk. Selsk. Mat. Fys. Medd. *34* (1965) No 14.
22. V. E. Viola, Jr., Nucl. Data Tables *A1* (1965) 391.
23. J. U. Andersen, K. Dan. Vidensk. Selsk. Mat. Fys. Medd. *36* (1967) No 7.
24. J. U. Andersen, O. Andreasen, J. A. Davies, and E. Uggerhøj, Radiat. Eff. *7* (1971) 25.
25. S. T. Picraux, in: *Ion Beam Surface Layer Analysis*, edited by O. Meyer, G. Linker, and F. Kappeln (Plenum, New York, 1976) 527.
26. Y. Hashimoto, J. H. Barrett, and W. M. Gibson, Phys. Rev. Lett. *30* (1973) 995.
27. H. E. Schiøtt, E. Bonderup, J. U. Andersen, and H. Esbensen, *Proc. 5th Int. Conf. on Atomic Collisions in Solids*, Gatlinburg, 1973 (Plenum, New York, 1975) 483.
28. J. U. Andersen and J. A. Davies, Nucl. Instrum. Methods *132* (1976) 179.
29. J. U. Andersen and L. C. Feldman, Phys. Rev. *B1* (1970) 2063.
30. S. U. Campisano, G. Foti, F. Grasso, I. F. Quercia, and E. Rimini, Radiat. Eff. *13* (1972) 23.
31. D. Gemmell, Rev. Mod. Phys. *46* (1974) 129.
32. T. Sikkeland, J. E. Clarkson, N. H. Steiger-Shafri, and V. E. Viola, Phys. Rev. *C3* (1971) 329.

33. I. Halpern and V. M. Strutinsky, *Int. Conf. on Peaceful Uses of Atomic Energy*, Geneva, vol. 15 (U.N., N.Y., 1958) 408.
34. J. U. Andersen, A. S. Jensen, E. Lægsgaard, K. O. Nielsen, J. S. Forster, I. V. Mitchell, D. Ward, and W. M. Gibson, to be published in Int. Symp. Phys. Chem. Fission, IAEA-SM/241-C7 (1979 IAEA: Jülich).
35. R. Bass, Nucl. Phys. *A231* (1974) 45.
36. J. E. Lynn, *Theory of Neutron Resonance Reactions* (Clarendon Press, Oxford, 1968) a) p. 325; b) p. 316.
37. J. E. Lynn, *Systematics for neutron reactions of the actinide nuclei*, Harwell Report 1974, AERE-R7468, p. 26.
38. S. Bjørnholm, A. Bohr, and B. Mottelson, Proc. Int. Symp. on Physics and Chemistry of Fission, Rochester, 1973; T. Døssing and A. S. Jensen, Nucl. Phys. *A222* (1974) 493.
39. M. Brack, T. Ledergerber, H. C. Pauli, and A. S. Jensen, Nucl. Phys. *A234* (1974) 185.
40. M. Brack, J. Damgaard, A. S. Jensen, H. C. Pauli, V. M. Strutinsky, and C. Y. Wong, Rev. Mod. Phys. *44* (1972) 320.
41. R. Vandenbosch and J. R. Huizenga, *Nuclear Fission* (Academic, New York, 1973) p. 184.
42. C. M. Perey and F. G. Perey, Atomic Data and Nuclear Data Tables *17* (1976) 1.
43. L. M. Bollinger, Proc. Int. Symp. on Nuclear Structure, Dubna (1968) p. 317.
44. J. W. Truran, A. G. W. Cameron, and E. Hilf, Int. Conf. on Properties of Nuclei far from the Region of Beta Stability, Leysin, Switzerland (1970) p. 275.
45. U. Mosel, Phys. Rev. *C6* (1972) 971.
46. W. D. Myers, *Droplet Model of Atomic Nuclei* (IFI/Plenum, New York, Washington, London, 1977).
47. A. V. Ignatyuk, M. G. Itkis, V. N. Okolovich, G. N. Smirenkin, and A. S. Tishin, Sov. J. Nucl. Phys. *21* (1975) 612.
48. R. Vandenbosch, Phys. Rev. *C7* (1973) 2092.
49. L. G. Moretto, S. G. Thomson, J. Routti, and R. C. Gatti, Phys. Letters *38B* (1972) 471.
50. M. E. Faber, A. Faessler, and M. Ploszajczak, Int. Symp. Phys. Chem. Fission, IAEA-SM/241-C5 (1979 IAEA: Jülich).

Indleveret til Selskabet september 1979.
Færdig fra trykkeriet april 1980